

RESONANCE STRUCTURE OF A PERIODICALLY FORCED DELAY DIFFERENTIAL EQUATION MODEL FOR THE EL NIÑO–SOUTHERN OSCILLATION

S. BOLDUC-ST-AUBIN, P. SUBRAMANIAN, AND B. KRAUSKOPF

ABSTRACT. We study resonance phenomena in the periodically forced Suarez–Schopf delay differential equation, which is a conceptual climate model for the El Niño–Southern Oscillation (ENSO). The system serves as a prototypical forced delayed-action oscillator whose self-sustained oscillations, when subjected to periodic forcing, give rise to attracting invariant tori. We provide a comprehensive bifurcation analysis of both the unforced and the forced model; for the latter, we propose a method to compute the rotation number of normally hyperbolic attracting invariant tori. With it we show that resonance tongues in parameter space are organized by critical points of the graph of the rotation number, both along torus bifurcation curves and within the region of invariant tori. We also show that the resonance structure repeats for large delays, which constitutes a reappearance mechanism not previously reported in the literature. Furthermore, depending on the feedback strength, we find bistability between period-one orbits and invariant tori. This regime involves non-classical bifurcation sequences, including ‘saddle-node’ and ‘gluing’ bifurcations of tori.

1. INTRODUCTION

The El Niño–Southern Oscillation (ENSO) is a complex and significant climate phenomenon that influences weather patterns globally [36]. Characterized by variations in sea surface temperatures (SSTs) and atmospheric pressure across the equatorial Pacific Ocean, ENSO manifests itself primarily in two phases: El Niño, with systematically warmer-than-average SSTs, and La Niña, with cooler-than-average SSTs in the eastern Pacific Ocean. These events have a profound impact on global climate, altering weather patterns, ocean conditions, and atmospheric pressure systems. Such changes can have widespread consequences for agriculture, water resources, and socioeconomic systems worldwide [39].

Figure 1 shows the time series of the Niño 3.4 index, a key indicator of El Niño and La Niña events. It illustrates the oscillatory nature of ENSO together with its marked irregularity in both amplitude and period, but with a seasonal phase: El Niño and La Niña events typically peak around December [50, 51].

The earliest explanations of ENSO date back to Bjerknes [8, 9], who identified the *Bjerknes positive feedback*: a warm SST anomaly in the eastern Pacific weakens the zonal SST gradient, reduces the Walker circulation [41] and easterly winds, and thereby promotes further eastward spreading of warm water. However, Bjerknes did not describe a mechanism capable of reversing this growth, making it clear that a *negative feedback* must oppose the warming (or cooling) phase [58].

Several conceptual frameworks formalize this interplay between positive and negative feedbacks, including the delayed action oscillator (DAO) [52, 6], the western Pacific oscillator [60, 59], the recharge–discharge oscillator [25, 24], and the advective–reflective

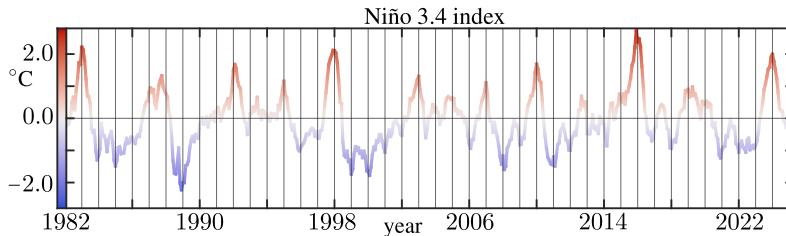


FIGURE 1. Niño 3.4 index time series taken from NOAA [14], which records SSTs anomalies in the central equatorial Pacific (5°N – 5°S and 170°W – 120°W). El Niño is defined as the index exceeding $+0.5^{\circ}\text{C}$ for at least five consecutive overlapping 3-month periods; La Niña occurs when it falls below -0.5°C over the same duration [56]. Peaks in the index occur near December, reflecting phase locking of ENSO variability to the seasonal cycle.

oscillator [42]. Each emphasizes a different pathway through which the system restores balance [59].

Conceptual frameworks like these condense the essential physics into manageable mathematical forms, facilitating analytical study and intuition building. This contrasts with large complex systems that model the oceans and atmosphere in considerable detail, and yet are much less amenable to mathematical discussion; see, e.g., [16] for a discussion of the role of conceptual climate models.

In this work, we focus on the DAO paradigm introduced by Suarez and Schopf [52]. Its underlying mechanism is illustrated schematically in Figure 2 and works as follows. Under normal conditions in the equatorial Pacific Ocean, easterly trade winds drive warm surface water toward the western equatorial Pacific, inducing upwelling in the east and establishing the Walker circulation. This zonal pattern produces warm, wet conditions in the west and cooler, drier conditions in the east. A perturbation that weakens the trade winds allows warm water to shift eastward. This perturbation generates propagating oceanic waves that travel along the thermocline – the transition zone between the warmer surface waters and the cooler deep waters. Westward-propagating Rossby waves reflect at the western boundary and return as Kelvin waves, providing a *negative delayed feedback* that ‘terminates’ the event. The perturbation also excites eastward-propagating Kelvin waves, providing a *positive delayed feedback* that is not included in the original DAO formulation, but has been considered by other authors [57].

Suarez and Schopf proposed a scalar delay differential equation for the ENSO DAO mechanism. In our notation, it takes the form

$$(1) \quad u'(t) = u(t) - u^3(t) - \alpha u(t - \tau),$$

which we refer to as the *Suarez and Schopf*, or simply, *S&S model* [19]. Here, $u(t)$ denotes a non-dimensional SST anomaly in the equatorial eastern Pacific; the nondelayed linear term captures the self-reinforcing nature of SST anomalies; and the cubic term acts as a nonlinear saturation mechanism. The delayed term $-\alpha u(t - \tau)$ models the negative feedback, of strength α and associated time delay τ , representing the overall travel time of the Rossby and Kelvin waves along the thermocline across the Pacific basin.

We note that the cubic term in the S&S model (1) was given little justification in the original work [52]. Later, Battisti and Hirst [6] provided qualitative support for this form, but without a mathematical derivation, making this model purely phenomenological. A significant advance was made by Falkena *et al.* [19], who derived S&S-type equations

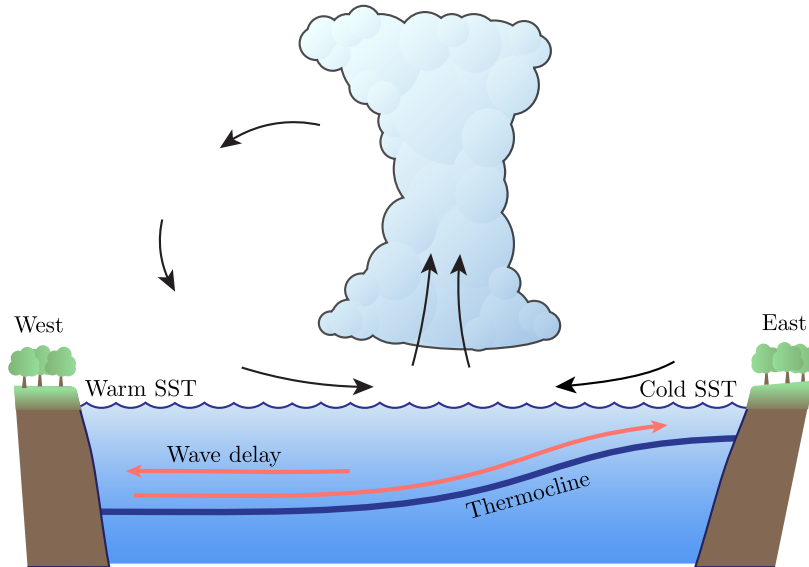


FIGURE 2. Sketch of a cross-section of the equatorial Pacific Ocean, where the blue line represents the thermocline. Oceanic waves (red arrows) travel west and east along the thermocline, creating a delayed negative feedback loop.

from a spatially extended ENSO model via two complementary reduction procedures (a variation of constants and the Mori–Zwanzig formalism [37, 64]). Both approaches recover essentially the same form of the system, featuring a cubic nonlinearity, but the precise structure of the delayed feedback terms differs slightly. Importantly, the original S&S model is retrieved from either formulation by setting a single parameter to zero, thereby placing it on a firm physical footing.

Motivated by the observation that ENSO events lock to the seasonal variation, several periodically forced DAO models have been considered and studied [57, 38, 10, 12, 33]. One of the most extensively studied conceptual ENSO models is the *Ghil-Zaliapin-Thompson (GZT) model* [21], which combines periodic forcing and a delayed feedback mechanism with a switching function as the nonlinearity. Early investigations of the GZT model relied primarily on numerical simulations [21, 62], while later work employed numerical continuation techniques (DDE-BifTool [47]) to clarify the structure of phase-locked solutions [29, 27]. Chaotic dynamics appear to be confined to relatively small regions of parameter space where resonance tongues overlap [29]. Extensions of the model that incorporate state-dependent delay [28] or asymmetric coupling function [30] were shown to exhibit substantially larger regions of resonance overlap and, correspondingly, more robust chaotic dynamics. We note that analytical insight has been obtained from piecewise-defined or reduced variants of the GZT model [44, 10].

Because the delayed negative feedback appears linearly, while nonlinearity acts locally through the cubic term, the S&S model is structurally more transparent than the GZT model. Moreover, in light of the recent derivations by Falkena *et al.* [19], the S&S model is no longer purely phenomenological but can be interpreted as a systematically reduced representation of spatially extended ENSO dynamics. These considerations provide strong justification for revisiting the S&S framework to study the role of periodic forcing for

observed dynamics. Namely, we study the system

$$(2) \quad u'(t) = u(t) - u^3(t) - \alpha u(t - \tau) + c \cos(\omega t),$$

where $\omega > 0$ is the angular frequency and $c > 0$ is the strength of the periodic forcing. We refer to Eq. (2) as the *periodically forced S&S* (pfS&S) model. Its formulation combines a physically motivated delayed feedback structure with explicit seasonal forcing. This combination of terms makes Eq. (2) relevant not only for climate modeling but also, more generally, for understanding the interaction between delayed feedback and periodic forcing.

In periodically forced delayed systems, such as the pfS&S and GZT models, intrinsic oscillations associated with delayed feedback interact with the external seasonal forcing, allowing for motion on invariant tori. Trajectories on these tori can be characterized by the *rotation number*, which represents the average number of rotations along one direction of the torus relative to the other. When the rotation number is rational, the dynamics is phase-locked; when the rotation number is irrational, the dynamics on the torus is quasiperiodic. In the former case, there are a stable and an unstable periodic orbit on the torus, and both form torus knots specified by the rational rotation number; see Section 4 for more details. In a two-parameter bifurcation diagram, phase-locked orbits form resonance tongues whose interplay can lead to complicated bifurcation scenarios and chaotic behaviour [31, 30].

The pfS&S model (2) has not yet been studied systematically. It was considered for angular forcing frequency $\omega = 1$ by Anikushin and Romanov [3], who reported regimes with positive maximal Lyapunov exponents, indicating chaotic dynamics for selected parameter values. With computer-assisted proof techniques, Oishi and Sekine [40] studied Eq. (2) for a wide range of angular frequencies ω . They proved the existence of large, overlapping resonance tongues and strong resonances, suggesting rich dynamical scenarios.

In this work we present a comprehensive bifurcation analysis of the pfS&S model. In contrast to earlier work, we focus our attention on the case $\omega = 2\pi$, where the forcing period is one. The modeling idea here is that Eq. (2) is expressed on a time scale of years. However, this is not obvious *a priori*; because it depends on the time-rescaling factor used to obtain the non-dimensionalised Eq. (1); we come back to this question in Section 7.

We begin with a bifurcation study of the unforced S&S model (1) in the (τ, α) -plane. We perform a linear stability analysis of the equilibria, which yields analytic expressions for the pitchfork and Hopf bifurcations. Bifurcations not captured by the linear stability analysis are studied with the continuation software DDE-BifTool [47]. Specifically, we find and continue saddle-node bifurcations of periodic orbits and homoclinic/gluing bifurcations. For sufficiently large delays, the only attracting invariant objects are periodic orbits.

We then analyse the bifurcations of the pfS&S model (2) in the (τ, c) -plane for the representative values of $\alpha = 1.25$ and $\alpha = 0.75$. The interaction between self-sustained oscillations and external forcing gives rise to invariant tori, and a key tool to study these dynamics is the rotation number. To compute it, we adapt the method of Bailie *et al.* [4, 5] — developed for periodically forced planar ODEs — to the delay setting, where the infinite-dimensional phase space requires suitable projections; this is described in Section 4. We show that resonance tongues in the (τ, c) -plane are very thin, indicating weak locking. Specifically, no resonance tongues overlap nor are period-doubling cascades observed. Nevertheless, interesting resonance structures appear: resonance tongues are organized not only by extrema of the rotation-number along torus bifurcation curves [54], but also by

critical points in the interior of the region with attracting invariant tori; this is consistent with recent observations in a periodically forced planar system [5]. For large delays, the resonance structure repeats periodically as described by rational map; at the level of the individual locked orbits, this corresponds to additional winding of the locked orbits along the longitudinal direction of the invariant torus. Moreover, symmetry-breaking bifurcations lead to complicated scenarios, including ‘folds of tori’ and ‘gluing bifurcations of tori’, in which invariant tori break up through a complex sequence of bifurcations. Despite this complexity, the overall dynamics — as studied via the headpoints on the stroboscopic section — closely parallel those of the unforced case.

We also briefly examine a periodically forced version of a physically motivated S&S-type equation derived by Falkena *et al.* [19] and show that it has effectively the same bifurcations and resonance structures; see Section 7. The only difference is that the resonance organization is richer: we find more critical points of the rotation number ρ both along the torus bifurcation curves and within the interior of the region of invariant tori.

The paper is organized as follows. Section 2 provides background on DDEs, dynamics on invariant tori, rotation numbers, and numerical methods for DDEs. In Section 3 we analyze the autonomous S&S model (1). In Section 4, we show that the pfS&S model admits motions to attracting invariant tori and introduce an algorithm to compute their rotation numbers. Section 5 presents a bifurcation analysis of the pfS&S model (2) with angular frequency $\omega = 2\pi$ for the cases $\alpha = 1.25$ and $\alpha = 0.75$. In Section 6, we study the reappearance mechanisms of the resonance tongues for large τ values. Finally, in Section 7 we briefly present for comparison the resonance structure of the periodically forced version of a model by Falkena *et al.* [19], discuss the role of varying the forcing frequency ω , and outline future directions.

2. BACKGROUND

We recall here some material underlying the analysis and numerical framework of our study.

2.1. Delay Differential Equations Formulation. Model (1) is an example of autonomous *delay differential equations* (DDEs), where the time derivative at the current time depends explicitly on the state of the system at earlier times. More specifically, Eq. (2) is a scalar DDE with a single constant delay τ of the form

$$(3) \quad u'(t) = f(u(t), u(t - \tau)), \quad f : \mathbb{R} \times \mathbb{R} \rightarrow \mathbb{R}.$$

An entire segment of the past trajectory is required as an initial condition, namely an initial function that specifies the state over $[-\tau, 0]$. Consequently, the phase space of a DDE of the form (3) is the infinite-dimensional space $\mathcal{C} := \mathcal{C}([-\tau, 0], \mathbb{R})$ of continuous functions over $[-\tau, 0]$ with values in \mathbb{R} . Given the right-hand side of (3) is locally Lipschitz continuous, the initial value problem with continuous initial data in \mathcal{C} admits a unique continuously differentiable solution $u(t)$ for some $t \geq 0$; see, e.g., [23, 49, 15]. For an initial function segment $\varphi \in \mathcal{C}$, the corresponding solution operator defines a continuous *semiflow*

$$S(t) : \mathcal{C} \rightarrow \mathcal{C}, \quad S(t)(\varphi) = u_t,$$

for some $t \geq 0$, on the Banach space \mathcal{C} equipped with the supremum norm; here $u(t) = u^\varphi(t)$ denotes the unique solution of (3) with initial condition φ , and $u_t \in \mathcal{C}$ is the state of the system at time t , defined in the usual way as

$$u_t(s) := u(t + s), \quad s \in [-\tau, 0].$$

In particular, $u_t(0) = u(t)$ and $u_t(-\tau) = u(t - \tau)$.

The infinite-dimensional phase space allows scalar DDEs with constant delays to exhibit a surprisingly rich range of dynamics, including sustained oscillations, chaotic behavior, and strong sensitivity to initial conditions; see, e.g., [18]. At the same time, the local stability theory of equilibria and periodic orbits is entirely analogous to that of *ordinary differential equations* (ODEs) since, as in ODEs, linearisations around equilibria and periodic orbits have at most finitely many unstable eigendirections [15]. Hence, classical bifurcation scenarios extend naturally to DDEs.

Their apparent simplicity in formulation paired with richness in behavior makes DDEs particularly appealing for exploring complex dynamical phenomena without resorting to overly large or computationally demanding models [31].

In the presence of periodic forcing, the DDE (3) takes the form

$$(4) \quad u'(t) = f(u(t), u(t - \tau), t), \quad f : \mathbb{R} \times \mathbb{R} \times \mathbb{S}^1 \rightarrow \mathbb{R},$$

where $f(\cdot, \cdot, t + 1) = f(\cdot, \cdot, t)$ is a periodic function whose period can be assumed to be 1 without loss of generality. Since system (4) is non-autonomous, the semiflow $S(t)$ no longer applies. Instead, one considers the two-parameter solution operator

$$S(t, t_0) : \mathcal{C} \rightarrow \mathcal{C}, \quad S(t, t_0)(\varphi) = u_t, \quad t \geq t_0,$$

where $u(t) = u^{\varphi, t_0}(t)$ is the unique solution of (4) with $u_{t_0} = \varphi$; see [23, 15]. The phase space is accordingly extended to $\mathcal{C} \times \mathbb{S}^1$, where \mathbb{S}^1 denotes the circle.

The theory of periodically forced DDEs is similar to that of periodically forced ODEs. In systems of the form (4), there are generally no equilibria, and the simplest attractors are period-one orbits. In particular, interactions between intrinsic oscillations and the periodic forcing generally leads to dynamics on a two-dimensional invariant torus $\mathcal{T} \cong \mathbb{S}^1 \times \mathbb{S}^1$. As for ODEs, trajectories lie on \mathcal{T} . For the DDE (4), this means that full history segments lie on the two-dimensional invariant torus \mathcal{T} .

A practical way to study the invariant objects of system (4) is to exploit the periodic forcing. We define the *stroboscopic map*

$$(5) \quad \mathcal{P}(\varphi; t_0) = S(t_0 + 1, t_0)(\varphi),$$

which maps the history segment $\varphi = u_{t_0}$ at time t_0 to the segment u_{t_0+1} one period later; the stroboscopic map acts on the infinite-dimensional space \mathcal{C} by identifying t_0 and $t_0 + 1$ (since $f(\cdot, \cdot, t)$ in (4) has period 1). Note that (5) is an example of a Poincaré map for the section $t = t_0$; in practice, one normally chooses $t_0 = 0$, and we simply write $\mathcal{P}(\varphi) = \mathcal{P}(\varphi; 0)$ from now on. Period-one orbits of system (4) correspond to fixed points of \mathcal{P} and, more generally, period- n orbits of (4) correspond to period- n points of \mathcal{P} , that is, fixed points of \mathcal{P}^n . Because the map \mathcal{P} acts on the infinite dimensional function space \mathcal{C} , projection methods are generally needed to visualize and study its invariant objects; see Section 4.

2.2. Motions on invariant tori and the rotation number. The stroboscopic map \mathcal{P} provides a natural framework for characterizing the dynamics on an invariant torus \mathcal{T} via the *rotation number*. Note that \mathcal{T} is two-dimensional, even though it lies in the infinite-dimensional phase space $\mathcal{C} \times \mathbb{S}^1$.

For periodically forced planar ODEs, an invariant torus \mathcal{T} defines an invariant closed curve \mathcal{I} of the stroboscopic map \mathcal{P} , on which \mathcal{P} acts as a circle map. The *rotation number* ρ is the limit of the average angular displacement per iterate along the invariant

closed curve \mathcal{S} ; see, e.g., [34]. The rotation number can equivalently be determined as the average of the oriented angular increments between consecutive iterates z_k of \mathcal{P} on \mathcal{S} :

$$(6) \quad \rho = \lim_{N \rightarrow \infty} \frac{1}{2\pi N} \sum_{k=0}^{N-1} \angle(z_k, Z, z_{k+1}),$$

where $\angle(z_k, Z, z_{k+1})$ denotes the oriented angle from z_k to z_{k+1} , taken in $(-\pi, \pi]$, with respect to a suitable reference point Z in the interior of \mathcal{S} ; note that ρ is independent of the choice of reference point, provided Z lies in the interior of (a projection of) the invariant closed curve \mathcal{S} ; see [5].

The rotation number ρ distinguishes two qualitatively different regimes:

- **locked dynamics:** when $\rho = p/q \in \mathbb{Q}$ (with p and q relative prime) then there are an attracting and a repelling periodic orbit on the torus, each of which forms a $p:q$ torus knot on \mathcal{S} .
- **quasiperiodic dynamics:** when $\rho \notin \mathbb{Q}$ then every trajectory on \mathcal{S} is dense, that is, never closes up.

Locked solutions are organized into resonance (or Arnold) tongues in parameter space, which are bounded by saddle-node bifurcations of periodic orbits [34]. Specifically, a $p:q$ resonance tongue emanates from a point on a torus bifurcation curve T where the critical Floquet multipliers are $e^{\pm i2\pi p/q}$. The critical Floquet multipliers change continuously along T ; moreover, resonance tongues are organized locally by the Farey tree [29]: the largest resonance tongue between those with rotation numbers p/q and ℓ/m is the one with rotation number $(p+\ell)/(q+m)$. Near the torus bifurcation curve T , the resonance tongues do not overlap; however, further away from T , neighboring resonance tongues may overlap, with associated breakdown of tori and possibly chaotic dynamics.

For DDEs, the invariant torus remains two-dimensional despite the fact that it now lies in an infinite-dimensional phase space. This is why the theory of resonance tongues carries over. Indeed, dynamics on invariant tori have been studied extensively for certain DDE models; see, e.g., [29, 18, 13, 54, 43]. This was achieved by finding the bounding curves SN of saddle-node bifurcation of periodic orbits of selected resonance tongues with continuation tools. The rotation number ρ , on the other hand, has not been considered for DDEs because computing it requires additional care, as we will see in Section 4.

2.3. Numerical tools. Several numerical tools are available for DDEs, and we use here a combination of numerical integration, continuation, and the computation of the rotation number ρ .

Time integration is important and has several uses in this work. We make use of the `dde23` [46] solver in MATLAB to compute the unstable manifold of an equilibrium, where our trajectories start in the unstable eigendirection of the equilibrium (which is provided by `DDE-BifTool`). We also compute the unstable manifold of a periodic orbit in a Poincaré section in a similar fashion; specifically, with the method detailed in [32], which requires several starting trajectories. Furthermore, we use `dde23` for finding stable solutions on tori, which are then used to find and continue the saddle-node bifurcations that bound resonance tongues in parameter space. To compute the rotation number, as detailed in Section 4, we perform extensive iterations by numerical integration of the stroboscopic map \mathcal{P} over a large parameter grid. For efficiency, we employ an Adams–Bashforth method [17] implemented in JULIA [7].

An essential tool we employ is the continuation software DDE-BifTool [47] in MATLAB [55]. The package DDE-BifTool is designed for autonomous systems. To apply it also to the non-autonomous system (4), such as system (2), we rewrite it as an autonomous system by introducing auxiliary equations that generate the periodic forcing. This is achieved by increasing the dimension of the system by two, to implement the Hopf normal form with an attracting unit circle; see [29]. DDE-BifTool enables the numerical continuation of equilibria and periodic orbits, as well as the continuation of bifurcations in one and two parameters. It also implements normal form computations, allowing, for instance, the determination of the criticality of Hopf bifurcations. The linear stability analysis also provides eigenvalues and associated eigenfunctions of the linearized problem. Furthermore, we continue saddle-node bifurcation of periodic orbits bounding resonance tongues and locate their root points along torus bifurcation curves by tracking the critical Floquet multipliers.

3. THE AUTONOMOUS S&S MODEL

The S&S model (1) is dissipative [2]. In particular, for $\alpha \in (0, 1)$, all trajectories of Eq. (1) are eventually attracted to the set $\{\varphi \in \mathcal{C} : \|\varphi\|_\infty \leq \sqrt{1 + \alpha}\}$; see [3]. Moreover, Eq. (1) has a natural \mathbb{Z}_2 -symmetry: if $u(t)$ is a solution then so is $-u(t)$. Consequently, the global attractor (which exists due to dissipativity) is invariant under the involution $u \mapsto -u$, or it consists of two parts that are each others image under the symmetry; the same holds for any other invariant sets.

3.1. Linear stability analysis. Equilibria of DDEs are constant functions in the space \mathcal{C} . Their stability analysis follows the classical approach for ODEs of linearizing the equation around the equilibrium. However, due to the presence of a delay term, the characteristic equation is transcendental rather than polynomial [49]. Nevertheless, bifurcations occur as parameters vary when characteristic roots cross the imaginary axis.

Proposition 1. [*Local bifurcations*]

For the autonomous S&S model (1) with parameters $\tau, \alpha > 0$, we have the following.

- (i) For $\alpha > 1$,

$$p_0 \equiv 0$$

is the only equilibrium, which is attracting for small τ .

- (ii) The equilibrium p_0 undergoes a pitchfork bifurcation $P(\tau, \alpha)$ along the line given by $\alpha = 1$; as α decreases through 1, the equilibria

$$p^\pm = \pm\sqrt{1 - \alpha}$$

emerge.

- (iii) For $0 < \alpha < 1$, the equilibrium p_0 is a saddle with a one-dimensional unstable manifold $W^u(p_0)$. The equilibria p^\pm are attracting for small τ .

- (iv) The equilibrium p_0 undergoes Hopf bifurcations $H_k(\tau_k, \alpha)$ at

$$(7) \quad \tau_k = \frac{\arccos(1/\alpha) + 2\pi k}{\sqrt{\alpha^2 - 1}}, \quad k \in \mathbb{N}_0.$$

Any periodic orbit $u(t)$ born at these Hopf bifurcations is symmetric, and satisfies

$$(8) \quad u(t) = -u(t + \frac{T}{2}),$$

where T is its (minimal) period. The principal branch $H_0(\tau_0, \alpha)$ marks the first loss of stability of p_0 as τ increases; $H_0(\tau_0, \alpha)$ is supercritical and the bifurcating periodic orbits is attracting for small τ . The curves $H_k(\tau_k, \alpha)$, $k \geq 1$, lie in the

region $\alpha > 1$ and have $\alpha = 1$ as an asymptote as $\tau \rightarrow \infty$, and $\tau = 0$ as an asymptote as $\alpha \rightarrow \infty$.

(v) The equilibria p^\pm undergo Hopf bifurcations $H_k^\pm(\tau_k^\pm, \alpha)$ at

$$(9) \quad \tau_k^\pm = \frac{\arccos((3\alpha - 2)/\alpha) + 2\pi k}{2\sqrt{(1 - 2\alpha)(\alpha - 1)}}, \quad k \in \mathbb{N}_0.$$

All periodic orbits born at these Hopf bifurcations come in pairs, related to each other by the symmetry (8). The principal branch $H_0^\pm(\tau_0^\pm, \alpha)$ marks the first loss of stability of p^\pm as τ increases; $H_0^\pm(\tau_0^\pm, \alpha)$ is subcritical and the bifurcating periodic orbit is a saddle. The curves $H_k^\pm(\tau_k^\pm, \alpha)$, $k \geq 1$, exist in the region $\frac{1}{2} < \alpha < 1$, and have asymptotes $\alpha = \frac{1}{2}$ and $\alpha = 1$ as $\tau \rightarrow \infty$.

(vi) There is a point DZ of double-zero bifurcation at $(\tau, \alpha) = (1, 1)$ on the curve P , here the linearisation has a double eigenvalue at zero, analogous to a Bogdanov–Takens bifurcation, but this occurs here in a system with \mathbb{Z}_2 -symmetry; see e.g. [48]. The curves H_0 , and H_0^\pm emerge from the point DZ. Because of the \mathbb{Z}_2 -symmetry of Eq. (1), the double-zero point DZ has the unfolding of the 1:2 resonance with $s = -1$ in Chapter 8 of [34].

For the proof see Appendix A.

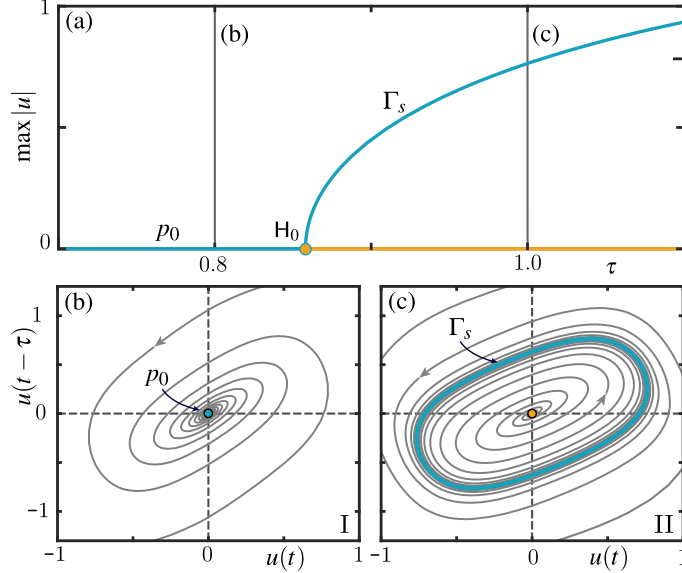


FIGURE 3. One-parameter bifurcation diagram in τ for $\alpha = 1.25$. Panel (a) shows the bifurcation diagram for $\tau \in [0.7, 1.1]$ in terms of the max-norm; attracting objects are blue, and saddles are orange. The equilibrium p_0 loses stability at H_0 , yielding the attracting periodic orbit Γ_s . Remaining panels show phase portraits in the $(u(t), u(t - \tau))$ -plane at $\tau = 0.8$ (b) and $\tau = 1.0$ (c), with representative trajectories (grey).

3.2. One-parameter bifurcation diagrams. To illustrate Proposition 1, Figure 3 and Figure 4 show one-parameter bifurcation diagrams in τ for fixed values of $\alpha = 1.25$ and $\alpha = 0.75$, respectively. In each figure, panel (a) presents the one-parameter bifurcation

diagram in τ with branches of solutions and associated bifurcations. The remaining panels show phase portraits in projections onto the $(u(t), u(t - \tau))$ -plane, with equilibria and periodic orbits, and some representative trajectories. For the case $\alpha = 0.75$, we also show the one-dimensional unstable manifold $W^u(p_0)$. In this projection, the \mathbb{Z}_2 -symmetry is evident: orbits are either invariant under a rotation by π about the origin, or they occur in symmetric pairs.

Figure 3(a) shows the one-parameter bifurcation diagram in τ for $\alpha = 1.25$, which has two regimes, labeled I and II. In regime I for small delay τ , the equilibrium p_0 is a global attractor, as seen in panel (b), where trajectories spiral toward p_0 . The supercritical Hopf bifurcation H_0 occurs at $\tau_0 \approx 0.8580$. From this bifurcation point emerges a branch of symmetric attracting periodic orbits Γ_s . The existence of Γ_s is a feature of regime II: as panel (c) shows, all trajectories converge to this symmetric periodic orbit.

Figure 4(a) shows the bifurcation diagram in τ for $\alpha = 0.75$. Compared with the previous case, the dynamics here are more intricate, and we distinguish the five distinct regimes III–VI. Panel (b) shows the phase portrait of regime III where the system exhibits the expected behavior following the pitchfork bifurcation P: the symmetric equilibria p^\pm are attracting, while p_0 is a saddle. The one-dimensional unstable manifold $W^u(p_0)$ has two sides, and one converges to p^+ and, by symmetry, the other converges to p^- . All other trajectories (not on the stable manifold of p_0) converge to either p^+ or p^- . As τ is increased, we encounter a bifurcation not covered by Proposition 1: a saddle-node bifurcation of periodic orbits SN_0 . The phase portrait in the ensuing regime IV, shown in panel (c), depicts an attracting outer orbit Γ_s and a repelling inner orbit Γ_u . Any trajectory inside Γ_u converges to either p^+ or p^- , while trajectories outside Γ_u converge to Γ_s . In particular, the unstable manifold $W^u(p_0)$ still converges to p^+ and p^- . At $\tau \approx 1.5903$, the inner periodic orbit Γ_u has shrunk and now connects to the saddle equilibrium p_0 , forming the figure-eight structure in Figure 4(d1). This homoclinic bifurcation is known as a *gluing bifurcation*, which we refer to as G. Here, both sides of the unstable manifold $W^u(p_0)$ return to the equilibrium p_0 ; see the enlarged view in panel (d2). The result of this gluing bifurcation is regime V, shown in panel (e), where a pair of repelling periodic orbits Γ_u^\pm exists. Both sides of $W^u(p_0)$ now converge to the attracting periodic orbit Γ_s , as do all other trajectories, except those inside the region enclosed by the pair Γ_u^\pm , which converge to either p^+ or p^- . For increasing τ , the repelling periodic orbits Γ_u^\pm shrink and eventually disappear at the subcritical Hopf bifurcations H_0^\pm at $\tau_0^\pm \approx 1.741$; its first Lyapunov coefficient is $l_1 \approx 2.9574$, indicating that the Hopf bifurcation is indeed subcritical. Beyond this point, in regime VI, shown in panel (f), the only remaining attractor is the periodic orbit Γ_s .

3.3. Two-parameter bifurcation diagram in the (τ, α) -plane. Figure 5 presents the bifurcation diagram of system (2) in the (τ, α) -parameter plane, over the ranges $\tau \in [0, 15]$ and $\alpha \in [0, 2]$. Shown are the bifurcation curves P, H_k and H_k^\pm from Proposition 1, together with the additional curves G and SN_0 identified in Figure 4. Solid curves in Figure 5 indicate bifurcations involving at least one attracting invariant object; they separate the plane into the regions I–VI defined in Section 3.2. Dashed curves represent bifurcations involving only saddle-type invariant objects; although the attractors themselves remain unchanged, saddle invariant objects may change or appear.

The pitchfork bifurcation P splits the (τ, α) -plane into two regions, with the equilibria p^\pm existing only for $0 < \alpha < 1$. Consequently, regions I–II are located above the line $\alpha = 1$, whereas regions III–VI are below it. On P, at $(\tau, \alpha) = (1, 1)$, lies the double-zero point DZ, from which the curves H_0 and H_0^\pm emanate, as stated in Proposition 1. The principal Hopf bifurcation curve H_0 separates regions I and II and approaches $\tau = 0$ as

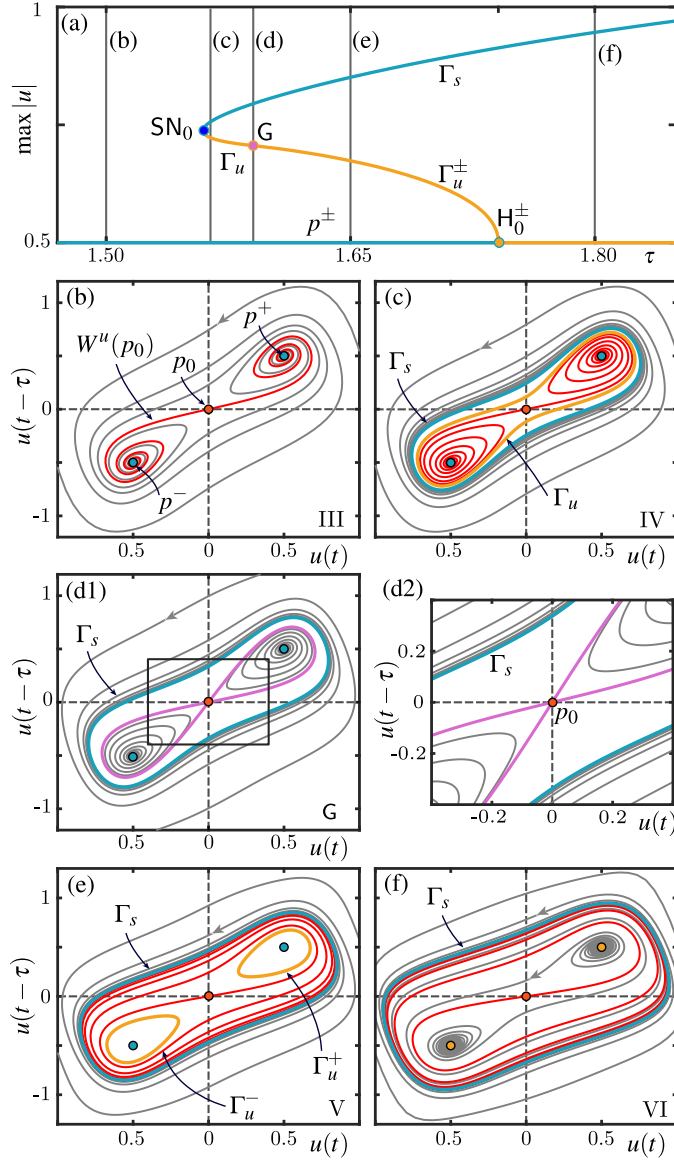


FIGURE 4. One-parameter bifurcation diagram in τ for $\alpha = 0.75$. Panel (a) shows the bifurcation diagram for $\tau \in [1.475, 1.85]$ in terms of the max-norm, with saddle-node bifurcation SN_0 , gluing bifurcation G and Hopf bifurcations H_0^\pm . Remaining panels show phase portraits in the $(u(t), u(t - \tau))$ -plane at $\tau = 1.5$ (b), 1.5656 (c), 1.5903 (d1), 1.65 (e) and 1.8 (f). Panel (d2) is an enlargement of panel (d1). Shown are: equilibrium p_0 (orange); equilibria p^\pm (blue when attracting, orange when saddle); attracting periodic orbit Γ_s (blue); saddle periodic orbits Γ_u and Γ_u^\pm (orange); unstable manifold $W^u(p_0)$ (red); homoclinic connection (purple); and representative trajectories (grey), with arrows showing the direction of the semiflow.

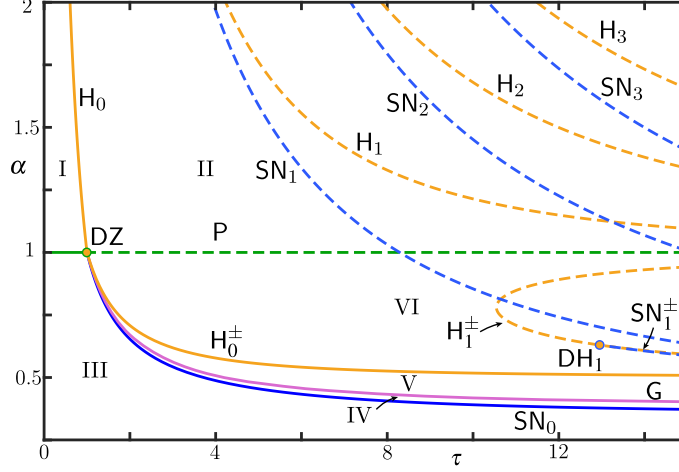


FIGURE 5. Bifurcation diagram of the S&S model (1) in the (τ, α) -plane showing the regimes I–VI; the curves of pitchfork bifurcation P, Hopf bifurcations H_k , H_k^\pm , fold bifurcations of periodic orbits SN_k , SN_k^\pm , and homoclinic/gluing G; and the codimension-two points DZ of double-zero bifurcation and DH_1 of degenerate Hopf bifurcation.

$\alpha \rightarrow \infty$. The Hopf bifurcation curve H_0^\pm tends to $\alpha = \frac{1}{2}$ as $\tau \rightarrow \infty$. From DZ also emerge the saddle-node of periodic orbit curve SN_0 and the gluing bifurcation curve G. Together, SN_0 , G, and H_0^\pm indeed separate the plane into the regions III–VI.

In regions II and VI, the only attracting object is the periodic orbit Γ_s . In region II, the Hopf bifurcation curves H_k , $k \geq 1$, are subcritical: the respective saddle periodic orbit that bifurcates from the equilibrium p_0 exists for smaller values of τ , and disappears at a saddle-node bifurcation curve SN_k . As stated in Proposition 1, the Hopf bifurcation curves H_k have asymptotes $\tau = 0$ as $\alpha \rightarrow \infty$ and $\alpha = 1$ as $\tau \rightarrow \infty$, respectively. The associated curves SN_k approach the same asymptote as $\alpha \rightarrow \infty$ but, at larger τ , they cross the line $\alpha = 1$ and enter region VI. In region VI, as τ increases, one encounters the sequence H_k^\pm , $k \geq 1$, of Hopf bifurcation curves. Each has a minimum in τ and asymptotes $\alpha = 1$ and $\alpha = \frac{1}{2}$ as $\tau \rightarrow \infty$. Along the curve H_1^\pm lies a degenerate Hopf bifurcation point DH_1 , at $(\tau, \alpha) \approx (12.95, 0.63)$, where the criticality of H_1^\pm changes. From DH_1 the saddle-node bifurcation curve SN_1^\pm emanates; however because additional unstable modes are present, no new attracting periodic orbit is created. This scenario repeats along each curve H_k^\pm , $k \geq 2$: each has a degenerate Hopf bifurcation point DH_k and saddle-node bifurcation curve SN_k^\pm ; these are all outside the range of Figure 5.

4. COMPUTATION OF THE ROTATION NUMBER

In this section, we extend the method proposed by Bailie *et al.* [4, 5], for computing the rotation number ρ of attracting invariant tori in periodically forced planar ODEs, to the case of a periodically forced DDE, specifically the pfS&S model (2).

4.1. Torus dynamics in the pfS&S model. Figure 6 presents a one-parameter bifurcation diagram in c for fixed $\tau = 2.7663$, $\alpha = 0.75$ and $\omega = 2\pi$. The value of τ is chosen because it corresponds to a local maximum in c of the torus bifurcation curve T in the (τ, c) -parameter plane (see already Figure 10). Figure 6(a) shows the rotation number ρ of

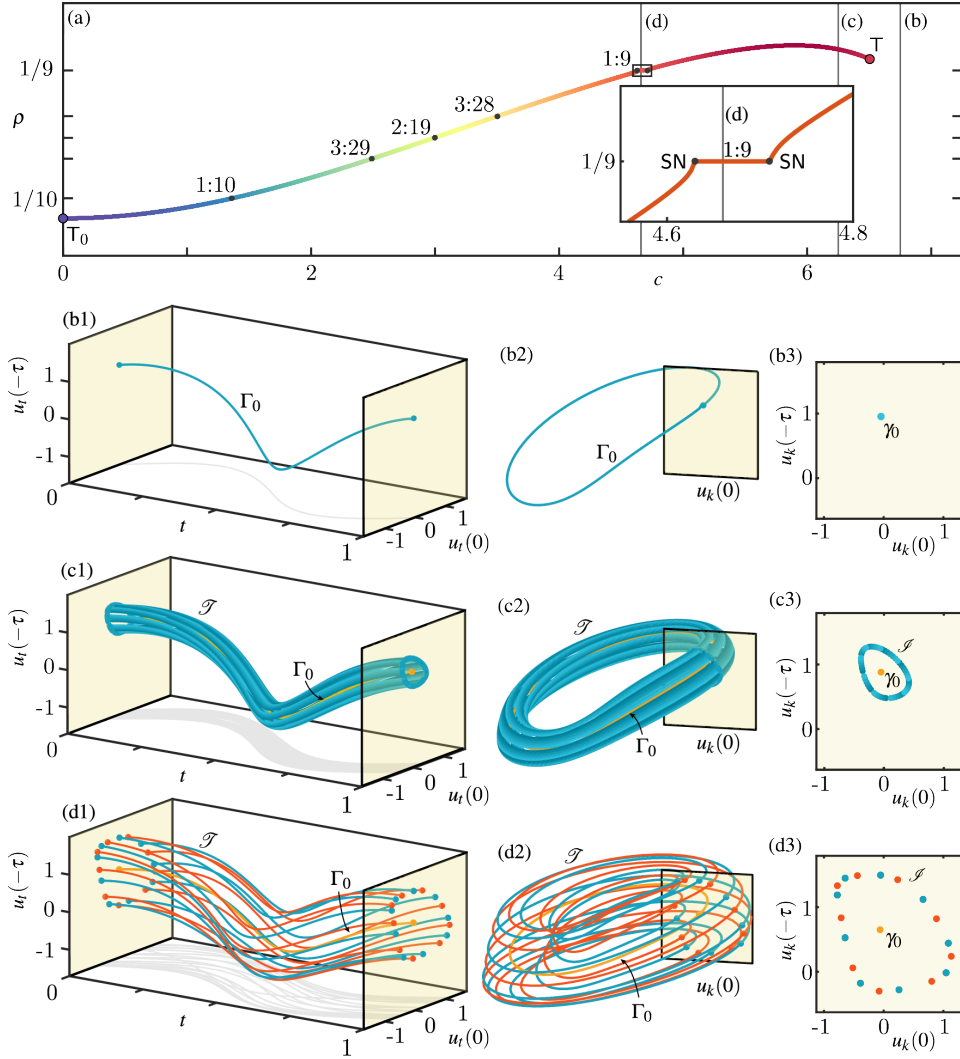


FIGURE 6. One-parameter bifurcation diagram in c for $\tau = 2.7663$, $\alpha = 0.75$ and $\omega = 2\pi$. Panel (a) shows the graph of ρ , between the torus bifurcations Γ_0 and Γ , and its inset enlarges ρ near the $1:9$ resonance tongue. Panels (b)–(d) illustrate representative dynamics: (b) attracting period-one orbit Γ_0 (blue) at $c = 6.75$; (c) attracting quasiperiodic orbit (blue) on the invariant torus \mathcal{I} with a 2-saddle period-one orbit Γ_0 (orange) at $c = 6.25$; (d) attracting and 1-saddle $1:9$ locked orbits (blue and red, resp.) on \mathcal{I} with a 2-saddle Γ_0 (blue) at $c = 4.66$. Columns (b1)–(d1) show trajectories represented in the $(t, u_t(0), u_t(-\tau))$ -space with the planes $t = 0$ and $t = 1$ identified, and columns (b2)–(d2) are their toroidal embedding in \mathbb{R}^3 . Columns (b3)–(d3) display the headpoints of the stroboscopic section (plane at $t = 0$), where the period-one orbit Γ_0 is a fixed point γ_0 of the stroboscopic map \mathcal{P} , and the headpoints of the orbits on \mathcal{I} lie on \mathcal{I} .

the normally hyperbolic attracting invariant torus \mathcal{T} that exists between the torus bifurcation \mathbb{T} at $c \approx 6.504$ and the point \mathbb{T}_0 at $c = 0$, where one finds a ‘trivial torus bifurcation’ when c is switched on. Selected resonance tongues are indicated by black dots on the graph of ρ . The two saddle-node bifurcations of periodic orbits SN bounding the larger 1:9 resonance tongue were detected with `DDE-BifTool`; they are shown more clearly in the inset. Rows (b)–(d) show representative dynamics: a period-one orbit Γ_0 , a quasiperiodic (or very long-period) orbit, and a pair of locked orbits on the invariant torus \mathcal{T} , respectively. Each column displays a different projection of the dynamics. In column (b1)–(d1), trajectories are represented in the three-dimensional $(t, u_t(0), u_t(-\tau))$ -space, with the planes $t = 0$ and $t = 1$. In column (b2)–(d2), these planes are identified to obtain an embedded torus in \mathbb{R}^3 . This is done by introducing $\theta = 2\pi t$ and applying the transformation

$$(10) \quad ((R + r u_t(0)) \cos(\theta), (R + r u_t(0)) \sin(\theta), r u_t(-\tau)),$$

where $R = 1.75$ and $r = 0.75$ control the major and minor radii of the torus. Column (b3)–(d3) shows the $(u_t(0), u_t(-\tau))$ -plane at $t = 0$ with headpoints of associated history segments. The period-one orbit Γ_0 defines the fixed point γ_0 of the stroboscopic map \mathcal{P} , and the invariant torus \mathcal{T} yields the invariant circle \mathcal{S} .

In Figure 6(a), the periodic forcing is dominating the dynamics for large c , and here the only attracting object is a period-one orbit Γ_0 ; the dynamic is seasonally dominated [10]. When c is decreased, the period-one orbit Γ_0 loses stability at the torus bifurcation \mathbb{T} , and an attracting invariant torus \mathcal{T} is born. The torus \mathcal{T} persists down to $c = 0$, where it ‘collapses’ onto the attracting periodic orbit Γ_s of the unforced system (1) at the trivial torus bifurcation \mathbb{T}_0 . The graph of ρ is a devil’s staircase—a piecewise constant and continuous, with plateaus at rational values corresponding to locked orbits (cross-sections of resonance tongues) and quasiperiodic motion in between. Each cross-section of a resonance tongue is bounded by a pair of saddle-node bifurcations of periodic orbits SN, and the largest, shown in the inset, is the 1:9 resonance tongue. The graph of ρ appears smooth elsewhere only because the remaining resonance tongues are too narrow to resolve.

Figure 6(b) shows the period-one orbit Γ_0 for $c = 6.75$, which appears as a single string in panel (b1), a closed loop in panel (b2), and the fixed point γ_0 of the stroboscopic map \mathcal{P} in panel (b3). After the torus bifurcation \mathbb{T} , the attracting invariant torus \mathcal{T} is born. The period-one orbit Γ_0 is now a saddle with two unstable Floquet multipliers; we say that it is a 2-saddle periodic orbit. Panel (c) shows a quasiperiodic orbit (or of very high period) at $c = 6.25$. The orbit densely fills \mathcal{T} , forming a cylinder in (c1) and a torus in (c2), where Γ_0 lies inside. In panel (c3), the headpoints in the $(u_t(0), u_t(-\tau))$ -plane form a smooth invariant closed curve \mathcal{S} that encircles γ_0 . Row (d) shows a pair of 1:9 locked orbits; an attracting periodic orbit and a saddle (1-saddle) periodic orbit winding around \mathcal{T} at $c = 4.66$. In the stroboscopic section of panel (d3), the attracting and saddle locked orbits each correspond to headpoints lying on \mathcal{S} , with the period-one point γ_0 inside it.

4.2. Computation of the rotation number. We introduce a method to compute the rotation number ρ of an attracting invariant torus \mathcal{T} for periodically forced DDEs (4) over a two-parameter grid, specifically, in the (τ, c) -plane for the pfS&S model (2). We focus on parameter regions near torus bifurcation curves, where one expects attracting invariant tori and resonance tongues. At each grid point, we integrate (4) from an initial condition and allow sufficient time for the trajectory to settle onto the attractor; we then compute ρ with the procedure presented below. To ensure that we follow the same attractor as parameters vary, we use parameter sweeping in a selected parameter by increasing it step-by-step and

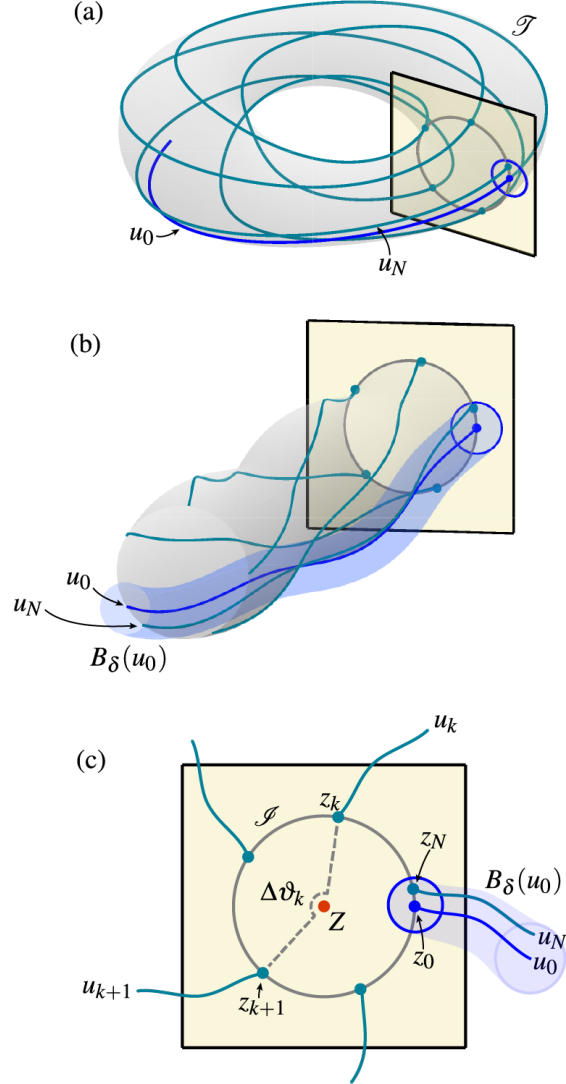


FIGURE 7. Schematic of the computation of the rotation number ρ for the periodically forced DDE (4). Panel (a) shows a trajectory $u(t)$ (green) winding around an attracting invariant torus \mathcal{T} (grey), which intersects the stroboscopic plane (yellow). Panel (b) illustrates how the stroboscopic map \mathcal{P} creates solution segments u_0, \dots, u_N . The index N is chosen so that $u_N \in B_\delta(u_0)$ (the blue cylinder). We show the corresponding headpoints $\{z_k\}$ in panel (c) with their history segments, as well as the reference point Z (red), from which we compute the oriented angular increments $\Delta\vartheta_k = \angle(z_k, Z, z_{k+1})$.

using the last function segment of the previous computation as the initial function for the next.

To compute the rotation number ρ at a given parameter point, we extend the method proposed by Bailie *et al.* [4, 5] for periodically forced planar ODEs, to periodically forced DDEs such as the system (2). This extension is motivated by Figure 6(c3)–(d3), which

shows that the headpoints of the stroboscopic sections in the $(u_t(0), u_t(-\tau))$ -plane lie on a smooth invariant closed curve \mathcal{S} , in close analogy with the planar case. This observation indicates that the stroboscopic map \mathcal{P} acts as a circle map on \mathcal{S} , and this allows us to adapt the method of [5]. The key idea is to iterate the Poincaré map until the final point is in a small neighborhood of the first point on \mathcal{S} . The rotation number ρ is then the average angular displacement, as in (6), over one full finite orbit of \mathcal{P} . Adapting this approach to the DDE setting faces two new difficulties. First, the return condition cannot be imposed solely on the headpoints in the Poincaré section, but must be formulated in the full function space \mathcal{C} to ensure that entire solution segments are close. Second, since the dynamics evolves in an infinite-dimensional space, a suitable projection onto \mathbb{R}^2 is required in order to define and compute the angle increments.

The method proceeds in four steps, illustrated in Figure 7, and we describe each in turn. We assume here that the torus \mathcal{T} bifurcates from a fixed point of \mathcal{P} (which can always be achieved by considering a higher iterate of \mathcal{P} if necessary).

Step 1: Transient integration. Given an initial function $\varphi \in \mathcal{C}$, and a fixed initial time $t_0 = 0$, we integrate (4) over a transient interval $[0, T_{\text{tr}}]$, where $T_{\text{tr}} \in \mathbb{N}$ is chosen large enough for the trajectory $u(t)$ to settle onto the attractor; see Figure 7(a). We refer to the first history segment on \mathcal{S} as u_0 .

Step 2: Stroboscopic iteration and return criterion. Starting from u_0 , we integrate (4) over successive time intervals $[T_{\text{tr}} + k - 1, T_{\text{tr}} + k]$ to generate a sequence of solution segments

$$u_k = \mathcal{P}(u_{k-1}), \quad k = 1, 2, \dots$$

in the section. This iteration stops at the first index N for which $u_N \in B_\delta(u_0)$, where $B_\delta(u_0)$ denotes the open ball in \mathcal{C} of radius $\delta > 0$ centered at u_0 . Measuring proximity in the full function space \mathcal{C} with the function norm $\|\cdot\|_{\mathcal{C}}$ ensures that entire solution segments are close; see Figure 7(b).

Three outcomes are possible. If $N = 1$, the trajectory has converged to a fixed point of \mathcal{P} , i.e., to a period-one orbit of (4), and the rotation number is undefined (the torus bifurcation has not yet taken place). If $N \leq N_{\text{max}}$, the return criterion is met: for a quasiperiodic orbit this is guaranteed by the density of the orbit on \mathcal{T} (and thus on \mathcal{S}); and for a $p:q$ locked orbit the return occurs exactly after q iterates. In either case we identify u_N with u_0 , thus, treating the orbit as N -periodic and closing it accordingly. If N_{max} is exceeded without the criterion being satisfied, we retain $u_{N_{\text{max}}}$ without closing the orbit and flag the instance for post-hoc inspection; the interpretation of such cases is discussed later.

Since we do not know a priori whether the orbit is locked or quasiperiodic, δ and N_{max} must be chosen to accommodate both cases. The tolerance δ is the primary tuning parameter: it controls the resolution of ρ by setting how tightly the orbit must close before N is accepted. A smaller δ resolves rotation numbers with larger denominators q and improves accuracy in the quasiperiodic case, but requires more iterates and, therefore, a larger N_{max} . The role of N_{max} is purely as a safeguard: it should be large enough to ensure that the return criterion is met under normal operation. The parameters δ and N_{max} must be tuned jointly to the required resolution, this depends on the system and the parameter region that is investigated.

Step 3: Projection onto the plane. The iterates $\{u_k\}$ lie on a smooth invariant curve $\mathcal{S}_{\mathcal{C}}$ in function space. We project them onto \mathbb{R}^2 via a map

$$\Pi: \mathcal{C} \rightarrow \mathbb{R}^2,$$

to obtain finite points

$$z_k = \Pi(u_k), \quad k = 0, 1, \dots, N,$$

which lie on the planar curve

$$\mathcal{S} = \Pi(\mathcal{S}_\ell) \subset \mathbb{R}^2.$$

Taking the headpoints in a specified Poincaré section as in Figure 6(b3)-(d3), is a natural choice for Π ; see [13, 32] for further discussion on suitable projections for DDEs.

Step 4: Angle summation. As reference point Z in the interior of \mathcal{S} , we take the componentwise mean of the projected points $\{z_k\}$ of the approximate N -cycle:

$$(11) \quad Z = \frac{1}{N} \sum_{k=0}^{N-1} z_k.$$

For each k , we then compute the oriented angle increment $\angle(z_k, Z, z_{k+1})$ between successive projected points; see Figure 7(c). The rotation number ρ is then computed by the finite Birkhoff sum

$$(12) \quad \rho = \frac{1}{2\pi N} \sum_{k=0}^{N-1} \angle(z_k, Z, z_{k+1}).$$

For periodic orbits, this finite sum is exactly the rotation number ρ ; for quasiperiodic orbits, it approximates ρ well for sufficiently large N .

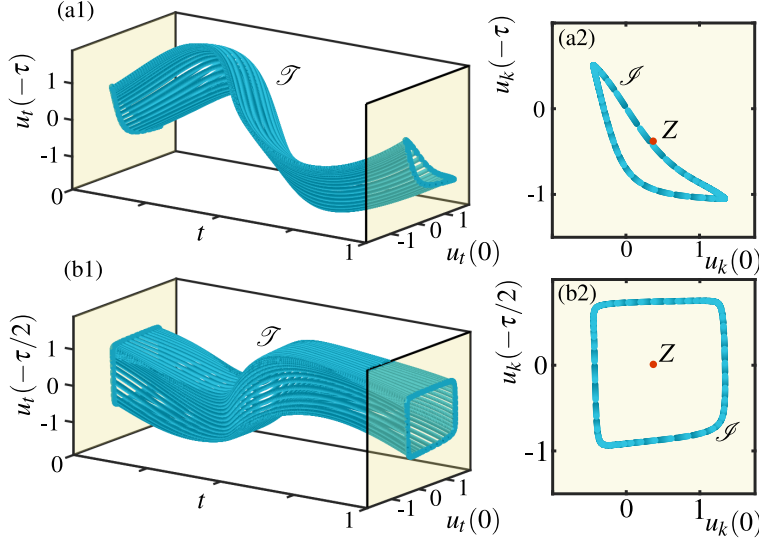


FIGURE 8. A single trajectory on a torus \mathcal{T} of the pfS&S model (2) with $\alpha = 1.25$, $c = 6.5$, $\tau = 9.11$ and $\omega = 2\pi$, shown in two different projections Π_1 and Π_2 in each row. Left column shows trajectories represented in $(t, u_t(0), u_t(-\tau))$ -space (top) and $(t, u_t(0), u_t(-\tau/2))$ -space (bottom), respectively. Right column shows the corresponding projected stroboscopic sections at $t = 0$ and the reference point Z with the invariant curve \mathcal{I} .

Because Step 4 of Algorithm 1 requires a two-dimensional setting to compute angles, one must then project from \mathbb{R}^3 onto \mathbb{R}^2 . As a practical choice, we consider the two projections

$$(13) \quad \Pi_1(\varphi) = (\varphi(0), \varphi(-\tau))$$

(the usual headpoints) and

$$(14) \quad \Pi_2(\varphi) = (\varphi(0), \varphi(-\tau/2))$$

(half-delay headpoints). The expectation is that at least one yields a well-shaped \mathcal{I} in \mathbb{R}^2 with Z in its interior; as we will see, this approach works well for the pfS&S model (2).

Past a torus bifurcation, the invariant circle \mathcal{I}_ℓ is small and the projection Π onto the headpoints of the stroboscopic section produces a simple and convex curve \mathcal{I} . This is illustrated in Figure 6(c3) and (d3) for the standard projection Π_1 in the $(u_t(0), u_t(-\tau))$ -plane. As parameters move away from the bifurcation, the torus grows and may distort, and the projected curve \mathcal{I} can become problematic; for instance, [13] reports a case where a projected invariant curve self-intersects to form a figure-eight. Figure 8 provides an example where the head-point projection Π_1 in row (a) fails, while Π_2 of the half-delay headpoints in row (b) yields a suitable projection. The left column (a1)–(b1) shows the trajectory in the $(t, u_t(0), u_t(-\tau))$ -space and $(t, u_t(0), u_t(-\tau/2))$ -space, respectively, from $t = 0$ to $t = 1$; and the right column (a2)–(b2) shows the corresponding headpoints forming \mathcal{I} with the centroid Z . While both curves are simple, the point Z computed with (11) lies outside the banana-shaped $\Pi_1(\mathcal{I}_\ell)$ in panel (a2). As a result, the infinite Birkhoff sum is zero, and we get a spurious value of $\rho = 6.59 \times 10^{-5}$. However, $\Pi_2(\mathcal{I}_\ell)$ in panel (b2) produces a simple closed curve with Z well inside it, and we obtain the value $\rho = 0.058$.

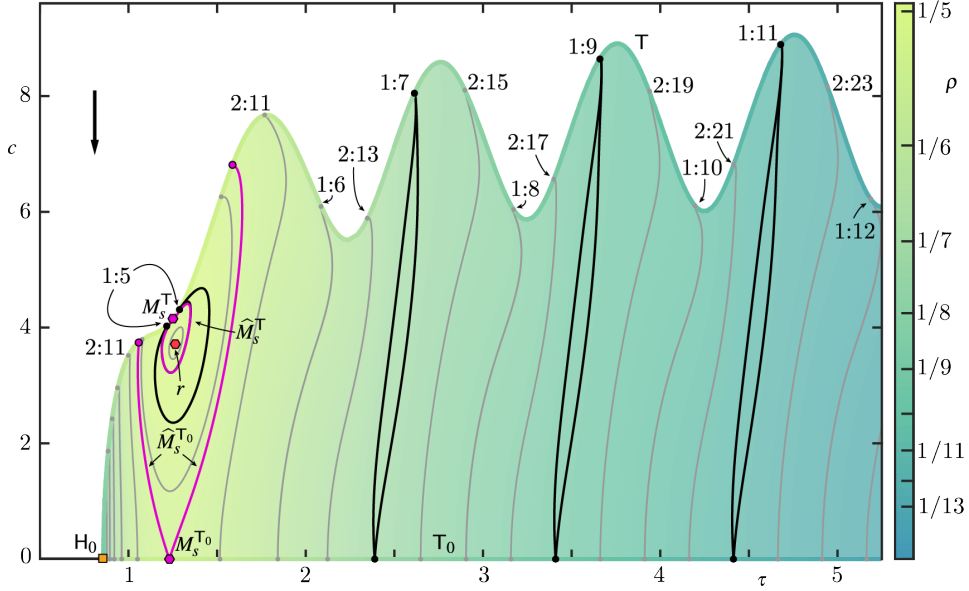


FIGURE 9. Bifurcation set and rotation number ρ of the pfS&S model (2) in the (τ, c) -plane for $\alpha = 1.25$ and $\omega = 2\pi$. In the white region, the period-one orbit Γ_0 is attracting, while in the coloured region the invariant torus \mathcal{S} is attracting, with the rotation number $\rho = \rho(\tau, c)$ indicated by the colorbar. This region is bounded by the torus bifurcation curves T and T_0 , which emanate from the Hopf bifurcation H_0 . We show $p:q$ resonance tongues and their root points of the form $1:q$ and $2:q$ in black and grey, as well as critical points of ρ . Boundary max-saddle points M_s^T and $M_s^{T_0}$, and their associated separatrices \widehat{M}_s^T and $\widehat{M}_s^{T_0}$, are shown in pink, and the interior maximum r in red.

Since it is not possible to determine beforehand where the standard projection Π_1 fails, we produce ρ for both projections Π_1 and Π_2 . At the end of the computation, we perform a diagnostic check of the continuity of ρ . If the continuity diagnostic reveals a jump discontinuity in ρ under one projection but not the other, this indicates a problem with the projection: the reference point Z may have drifted outside \mathcal{S} . We then discard the projection that returns an approximate value of 0 and keep the other one. This ensures a consistent computation of ρ throughout the parameter region, as shown in Figures 9 and 10.

The computation of the rotation number ρ of a DDE in parameter space is expensive. For instance, the grid in the (τ, c) -plane for the pfS&S model (2) shown in Figure 9 requires 768,000 rotation number computations in total, taking approximately 8 hours with the third-order Adams–Bashforth method in Julia without parallelization on an Apple M1 (16 GB).

5. BIFURCATION ANALYSIS OF THE PFS&S MODEL

We now analyze the torus dynamics of the pfS&S model (2) in the (τ, c) -plane for forcing frequency $\omega = 2\pi$. To this end, we first consider in Section 5.1 the simpler case that $\alpha = 1.25$. We then present in Section 5.2 the resonance structure for the richer and more physically relevant case $\alpha = 0.75$.

5.1. Case $\alpha = 1.25$. Figure 9 shows the bifurcation diagram of Eq. (2) in the (τ, c) -plane for $\omega = 2\pi$ and $\alpha = 1.25$. The torus bifurcation curve T emerges from the supercritical Hopf bifurcation H_0 near $(\tau, c) \approx (0.8580, 0)$, which is the Hopf bifurcation H_0 of the unforced system (1) from Proposition 1(iv). The curve T separates the (τ, c) -plane into two regions. Above T , the seasonal forcing dominates and the period-one orbit Γ_0 is attracting; below it, Γ_0 is a saddle period-one orbit and an attracting invariant torus \mathcal{T} exists. This region with an attracting torus is bounded by the torus bifurcation curves T and T_0 (with $c = 0$), and it extends seemingly periodically to arbitrarily large values of τ . The rotation number ρ in this region is computed with Algorithm 1 with downward sweeps in c for fixed values of τ , and it is illustrated in color according to the colorbar. Along the torus bifurcation curves T and T_0 , the torus does not yet exist, but the rotation number ρ is still well-defined. At T , the critical Floquet multipliers are $e^{\pm 2\pi i \kappa}$, and $\rho = \kappa$ (or $\rho = 1 - \kappa$) serves naturally as the rotation number. At T_0 , the rotation number is defined as the ratio of the forcing period and the natural period T of the autonomous periodic orbit Γ_s from Eq. (1); since the forcing frequency is $\omega = 2\pi$ (period 1), this gives $\rho = 1/T$. Importantly, ρ varies smoothly along the torus bifurcation curves T and T_0 , allowing us to locate resonance points at its rational values. In Figure 9, we marked with dots all $p:q$ resonance points of the form $1:q$ and $2:q$, of which there are finitely many because the rotation number ρ is bounded away from zero; these serve as root points of the associated shown resonance tongues. The boundaries of larger resonance tongues (black) are obtained with `DDE-BifTool` by tracking saddle-node bifurcations `SN` of the pair of locked orbits. The remaining resonance tongues (grey) are found as level sets of ρ .

In Figure 9, the resonance tongues do not overlap; that is, an attracting invariant and normally hyperbolic torus \mathcal{T} exists throughout the colored region. Hence, the graph of $\rho = \rho(\tau, c)$ is defined and continuous everywhere in the region, and it has the following properties: for every rational value of ρ , there exists a plateau of locked orbits – a resonance tongue – containing an attracting and a saddle periodic orbit. Quasiperiodic motion occurs at irrational values of ρ between the plateaus. Thus, the graph of ρ is piecewise constant, reminiscent of a devil’s staircase but extended to two parameters, for which the name *devil’s terraces* has been coined [26, 5]. For all rational values of the rotation number ρ , we find root points of resonance tongues on the torus bifurcation curve T_0 , all of which connect to corresponding root points on the torus bifurcation curve T . On T_0 , the supercritical Hopf point H_0 is a local minimum of ρ , from which ρ increases as τ increases until reaching a local maximum $M_s^{T_0}$; for larger τ , the rotation number ρ decreases again. This local maximum $M_s^{T_0}$ plays a special role: it is associated with two separatrix level sets $\widehat{M}_s^{T_0}$ along which ρ is constant, each connecting to T at the corresponding value of ρ . Along T , we similarly identify a local maximum M_s^T , where the value of ρ at M_s^T is larger than at $M_s^{T_0}$. The separatrix \widehat{M}_s^T connects to itself at the point M_s^T to form a closed loop.

The organization of resonance tongues around extrema of ρ on torus bifurcation curves was studied by Terrien *et al.* [54]. Building on this, Bailie *et al.* [4, 5], working with a periodically forced planar ODE, extended this picture into the interior of the region of attracting invariant tori by applying a Morse-theory inspired framework for determining the structure of the graph of ρ . In this framework, critical points of ρ — both on the torus bifurcation curves T and T_0 and in the interior of the resonance region — are classified as maxima, minima, or saddles. The local maxima M_s^T and $M_s^{T_0}$ of ρ on the torus bifurcation curves act as boundary saddles of the resonance region [5], and their separatrices \widehat{M}_s^T and $\widehat{M}_s^{T_0}$ partition the resonance region, grouping resonance tongues into families according to which side of the separatrix they lie on. In Figure 9, we identify an interior maximum r of

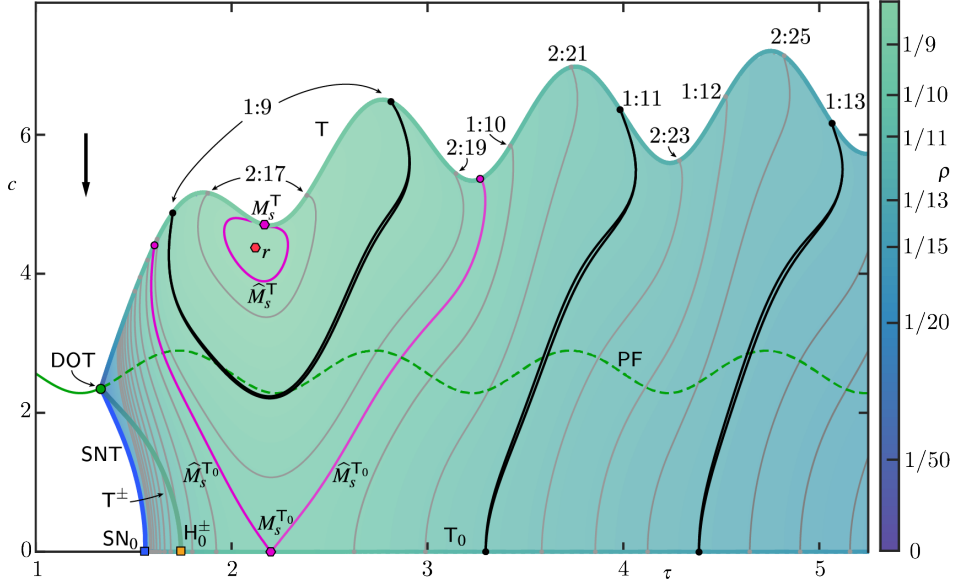


FIGURE 10. Bifurcation set and rotation number ρ of the pfS&S model (2) in the (τ, c) -plane for $\alpha = 0.75$ and $\omega = 2\pi$. In the white region, above the pitchfork of period-one orbits PF in green, the period-one orbit Γ_0 is attracting, and the period-one orbits Γ^\pm are attracting below it. In the coloured region, the invariant torus \mathcal{T} is attracting, with the rotation number ρ indicated by the colorbar, which reaches zero at the double-one bifurcation of tori point DOT. This region is bounded by the torus bifurcation curves T and T_0 and the locus of SNT. We show $p:q$ resonance tongues and their root points of the form $1:q$ and $2:q$ with $q \leq 50$ in black and grey, as well as critical points of ρ : boundary max-saddle points M_s^T and $M_s^{T_0}$, and their associated separatrices \widehat{M}_s^T and $\widehat{M}_s^{T_0}$, are shown in pink, and the interior maximum r in red. Along $c = 0$, we show the saddle-node of periodic orbit SN_0 , the gluing bifurcation G, and the subcritical Hopf bifurcations H_0^\pm .

ρ , located away from the torus bifurcation curves: it is a plateau if $\rho(r)$ is rational, or an isolated point if $\rho(r)$ is irrational. Overall, the critical points of ρ organizes the resonance tongues into four families. Resonance tongues contained within the region enclosed by \widehat{M}_s^T form annulus-like structures surrounding the interior maximum r ; in particular, they are not rooted to any torus bifurcation curve. Resonance tongues outside this region but within the domain bounded by $\widehat{M}_s^{T_0}$ and T, such as the 1:5 resonance tongue, possess two root points on T, one on each side of M_s^T . Finally, all resonance tongues lying outside this domain entirely, such as the 2:11 resonance tongue, are attached to T on one side and to T_0 on the other; these are distinguished as two families, one on either side of $\widehat{M}_s^{T_0}$, as discussed above.

For sufficiently large τ (above 2), the torus bifurcation curve T oscillates in c with period one in τ , and seems to converge to a sine wave with c ranging between about 6 and 9. Moreover, the entire resonance structure also appears to repeat with period one in τ : for example, the 1:7 resonance tongue closely resembles the 1:9, 1:11, and higher odd-denominator tongues, each shifted by one in τ . This self-similar reappearance mechanism is studied in detail in Section 6.

5.2. Case $\alpha = 0.75$. We now turn to the more physically relevant and more complex case $\alpha = 0.75$. Figure 10 shows the two-parameter bifurcation diagram of Eq. (2) in the (τ, c) -plane for fixed $\omega = 2\pi$ and $\alpha = 0.75$ with the graph of ρ represented again by color according to the colorbar. The first impression is that the resonance structure is very similar to that of Figure 9. There are torus bifurcation curves T and T_0 with boundary saddles M_s^T and $M_s^{T_0}$, their associated separatrices \widehat{M}^T and \widehat{M}^{T_0} , and the interior maximum r ; together, these govern the overall resonance structure shown in Figure 9. For large delays τ , the resonance structure also repeats, as we will discuss in Section 6.

However, the overall dynamical landscape in Figure 10 is considerably richer, because there are additional bifurcation curves and codimension-two points for $\alpha = 0.75$: the pitchfork bifurcation of period-one orbits PF, a pair of torus bifurcation curves T^\pm , and the double-one torus bifurcation point DOT. Along the zero-forcing line ($c = 0$), we also indicate the subcritical Hopf bifurcations H_0^\pm , the gluing bifurcation G, and the fold of periodic orbits SN_0 of the autonomous system (1). Note that the value of the rotation number ρ at the double-one torus bifurcation point DOT reaches zero. This is why we show the $p:q$ resonance tongues of the form $1:q$ and $2:q$ again, but now only for $q \leq 50$; notice how the shown resonance tongues accumulate near the point DOT.

In Figure 10, the pitchfork bifurcation PF separates the (τ, c) -plane into two regions. Above PF, there exists a single symmetric attracting periodic orbit Γ_0 of period $T = 1$. Below PF, there exists a pair of symmetry-related periodic orbits Γ^\pm (also of period $T = 1$) and Γ_0 is now unstable. At $(\tau, c) \approx (1.344, 2.370)$ on PF lies the double-one bifurcation of tori point DOT, where two nontrivial Floquet multipliers are equal to $+1$. This is a codimension-two bifurcation whose unfolding at the level of a Poincaré section is that of the 1:2 strong resonance [34]. From DOT emanate three torus bifurcation curves: the curve T above PF, where Γ_0 loses stability and an attracting invariant torus \mathcal{T} is born, and the curve T^\pm below PF, where Γ^\pm lose stability to create a pair of saddle-type invariant tori. The torus bifurcation curve T behaves analogously to the case $\alpha = 1.25$: as τ increases, it converges to a nearly sinusoidal shape with period one in τ . The curve T^\pm , on the other hand, connects to the zero-forcing line, at the subcritical Hopf bifurcation point H_0^\pm . After a ‘gluing bifurcation’ of the saddle-type invariant tori, the resulting single saddle torus merges with the attracting torus \mathcal{T} at a ‘saddle-node of tori’ SNT; see Section 5.2.1 for details. Crucially for now, the region with attracting invariant torus \mathcal{T} in Figure 10 is bounded by the torus bifurcation curves T and T_0 , and the locus SNT.

5.2.1. Bistability of tori for small τ . Figure 11 shows an enlargement of Figure 10 in the region $(\tau, c) \in [1.2, 1.8] \times [0, 5]$, centered around the double-one bifurcation point DOT. In panels (a) and (b), the values of the rotation number ρ are obtained by sweeping τ in opposite directions for fixed values of c ; this reveals a region of bistability between the attracting invariant torus \mathcal{T} and the period-one orbits Γ^\pm . In addition to the torus bifurcation curves T and T^\pm , it shows bifurcation loci emanating from the bifurcation point DOT: the locus SNT of ‘saddle-nodes of tori’, which connects to the point SN_0 at $c = 0$, and the locus GT of ‘gluing bifurcation of tori’, which connects to the point G at $c = 0$.

The bistability region in Figure 12 is bounded by the locus SNT, and the curves T_0 and T^\pm , and contains the locus GT in its interior. Near SNT, the attracting invariant torus \mathcal{T} and a saddle-type invariant torus \mathcal{T}_s ‘collide’ and annihilate. Near GT, a pair of saddle-type tori \mathcal{T}_s^\pm ‘merge’ into a single saddle-type torus \mathcal{T}_s . We stress that these loci are not smooth bifurcation curves: theory predicts that the collision or merging of tori is preceded

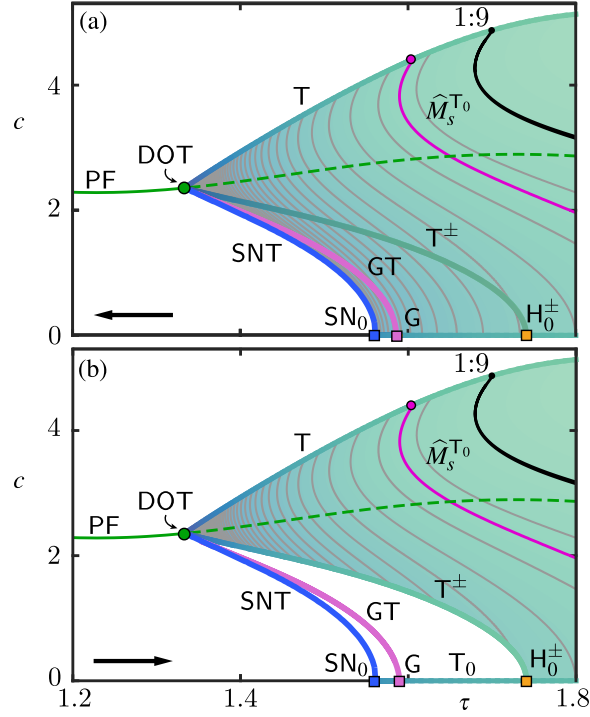


FIGURE 11. Enlarged view of the bifurcation diagram from Figure 10 showing the region of bistability bounded between the locus SNT of the saddle-node of tori and torus bifurcation curves T^\pm and T_0 . The rotation number ρ is given according to the color scheme shown in Figure 10 as c is fixed and τ is swept to the left in (a) and to the right in (b). Also shown is the locus GT of the gluing bifurcation of tori.

by a loss of normal hyperbolicity and a sequence of torus breakdown events involving global bifurcations such as homoclinic tangencies; see, e.g., [27].

We now look at the transition through the bistability region more closely. Figure 12 shows a one-parameter bifurcation diagram in τ for $c = 1$, that is, along the corresponding slice of Figure 11. Figure 12(a) presents, in terms of the maximum of the solution $u(t)$, the period-one orbits Γ^\pm and the invariant torus \mathcal{I} . The stable branch of \mathcal{I} above the point SNT was found by integration with parameter sweeping; note that large resonance tongues appear as ‘local dips’ because the locked solution does not attain the maximum value of $u(t)$ on the torus \mathcal{I} ; see [29]. The branch of saddle tori between SNT and T^\pm cannot be found by forward integration; it is represented here by selected $p:q$ locked saddle periodic orbits. Each of these periodic orbits was continued in the (τ, c) -plane from the zero-forcing line up to $c = 1$. The inset shows an enlargement near GT, where the symmetric pair of invariant tori \mathcal{I}_s^\pm ‘merges’ to form a single torus \mathcal{I}_s . The remaining panels show representative phase portraits of the stroboscopic Poincaré map as the headpoints in the $(u_t(0), u_t(-\tau))$ -plane. Here, the period-one orbits Γ_0 and Γ^\pm are represented by the fixed points γ_0 and γ^\pm , and the invariant torus \mathcal{I} , and the saddle-type tori \mathcal{I}_s and \mathcal{I}_s^\pm , by the invariant circles \mathcal{I} , \mathcal{I}_s and \mathcal{I}_s^\pm respectively. The invariant circles \mathcal{I}_s^\pm and \mathcal{I}_s are found

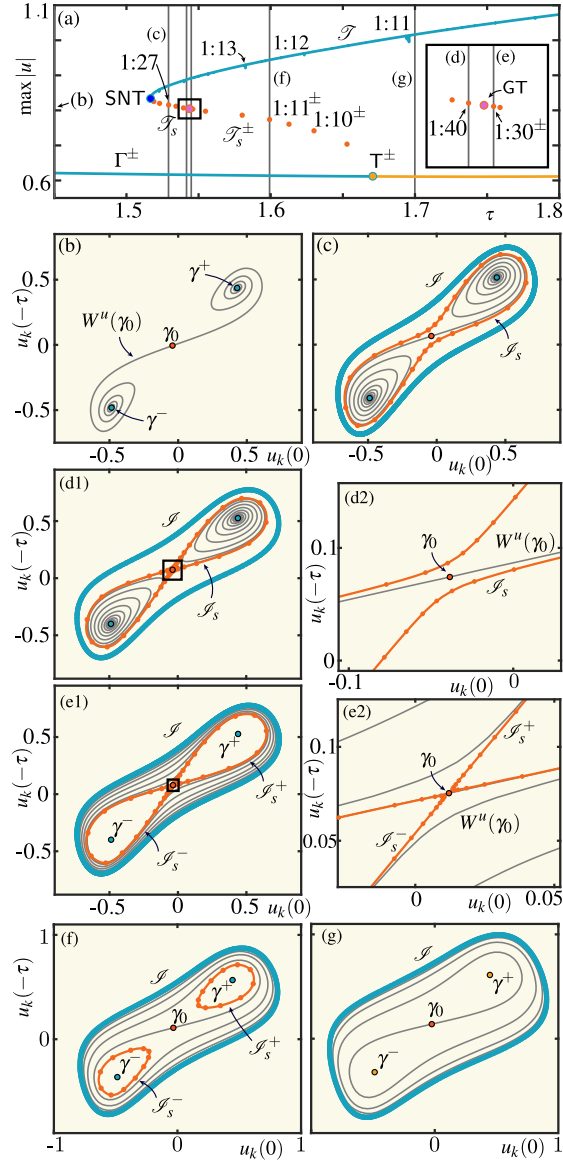


FIGURE 12. One-parameter bifurcation diagram in τ for $\alpha = 0.75$, $\omega = 2\pi$ and $c = 1$. Attracting objects are in blue, 1-saddles in yellow, and 2-saddles in orange. Panel (a) shows the bifurcation diagram in τ in terms of the max-norm. The attracting period-one orbits Γ^\pm and attracting invariant torus \mathcal{S} are shown, and the branches of saddle-type invariant tori \mathcal{S}_s and \mathcal{S}_s^\pm are represented by selected locked orbits. The inset zooms in on the gluing bifurcation GT. Remaining panels show the projected headpoints of the relevant invariant objects in the stroboscopic section for $\tau = 1.45$ (b), 1.5292 (c), 1.5418 (d1), 1.5451 (e1), 1.5992 (f), 1.7 (g), where a period-one orbit Γ becomes a fixed point γ , and the headpoints of a locked-orbit on a torus \mathcal{S} lie on invariant circle \mathcal{S} . Panels (d2)–(e2) are enlargement of panels (d1)–(e1). Also shown is the unstable manifold $W^u(\gamma_0)$ (grey).

by computing the respective locked orbit on them and then completing the invariant curve via spline interpolation. We also plot the one-dimensional unstable manifold $W^u(\gamma_0)$.

For small values of τ , as in Figure 12(b), the fixed point γ_0 is a saddle and γ^\pm are attracting. The unstable manifold $W^u(\gamma_0)$ has two branches that converge to γ^+ and γ^- , respectively. As τ increases past the saddle-node of tori SNT at $\tau \approx 1.5175$, the system now has an attracting torus \mathcal{T} and a saddle-type torus \mathcal{T}_s . The resulting phase portraits of \mathcal{P} is shown in panel (c), with the outer attracting invariant circle \mathcal{I} and the inner saddle invariant circle \mathcal{I}_s . Note that the dynamics on \mathcal{T} is quasiperiodic (or of very high period), while on \mathcal{T}_s there is a 1:27 locked orbit. At $\tau = 1.5418$, we obtain a topologically equivalent scenario to panel (c), but with a 1:40 locked orbit on \mathcal{T}_s . The associated saddle invariant circle \mathcal{I}_s , shown in panel (d1), approaches the fixed point γ_0 closely; this is seen more clearly in the enlargement panel (d2). As τ is increased past GT, the single saddle-type torus \mathcal{T}_s splits into a conjugate pair \mathcal{T}_s^- and \mathcal{T}_s^+ . The phase portraits of \mathcal{P} at $\tau = 1.5451$, shown in panel (e1), displays the associated invariant circles \mathcal{I}_s^+ and \mathcal{I}_s^- , each represented by a 1:30 locked orbit; note that \mathcal{I}_s^\pm come extremely close to the fixed point γ_0 , even in the enlargement panel (e2). As τ is increased further to $\tau = 1.5992$, as in panel (f), the saddle invariant circles \mathcal{I}_s^\pm , now represented by 1:11 locked orbits, have shrunk sufficiently to be clearly distinguished from one another. For increasing τ , the saddle-type tori \mathcal{T}_s^\pm continue to shrink, and they eventually disappear at the pair of subcritical torus bifurcations T^\pm at $\tau \approx 1.672$. Beyond this point, illustrated in panel (g) for $\tau = 1.7$, the periodic orbits Γ^\pm are of saddle type and the attracting torus \mathcal{T} , whose invariant circle \mathcal{I} remains densely filled, is globally attracting.

We conclude that the one-parameter bifurcation diagram of Figure 12 closely mirrors the transitions found in the unforced S&S model (1) shown in Figure 4. Observe that the double-one torus bifurcation DOT acts as an organizing center for the bifurcations of tori in Figure 11, in direct analogy with DZ organizing the bifurcations of periodic orbits of (1) in Figure 5. Under periodic forcing, equilibria p_0 and p^\pm lift to period-one orbits Γ_0 and Γ^\pm , and their bifurcations lift accordingly: bifurcations of equilibria become bifurcations of periodic orbits, and bifurcations of periodic orbits become bifurcations of invariant tori. This correspondence is summarized in Table 1.

TABLE 1. Analogy between bifurcations of the autonomous system (1) and the periodically forced system (2).

autonomous	periodically forced
Pitchfork of equilibria P	Pitchfork of period-1 orbits PF
Hopf bifurcations H_0, H_0^\pm	Torus bifurcations T, T^\pm
Fold of periodic orbits SN_0	‘Fold of tori’ SNT
gluing of periodic orbits G	‘gluing of tori’ GT
Double-zero bifurcation DZ	Double-one bifurcation of tori DOT

In particular, we find no evidence of torus breakdown near the ‘bifurcations’ SNT or GT: although theory guarantees that homoclinic tangencies and torus break-up must occur, the interval over which they do so is exponentially small in the frequency ratio. Owing to the very small rotation number in this region, we observe that those structures near SNT and GT lie beyond numerical detectability. The loci SNT and GT can therefore be treated as smooth curves for all practical purposes. We located SNT by sweeping τ leftward for each fixed c and identifying the rightmost value at which a torus is still found; here, we

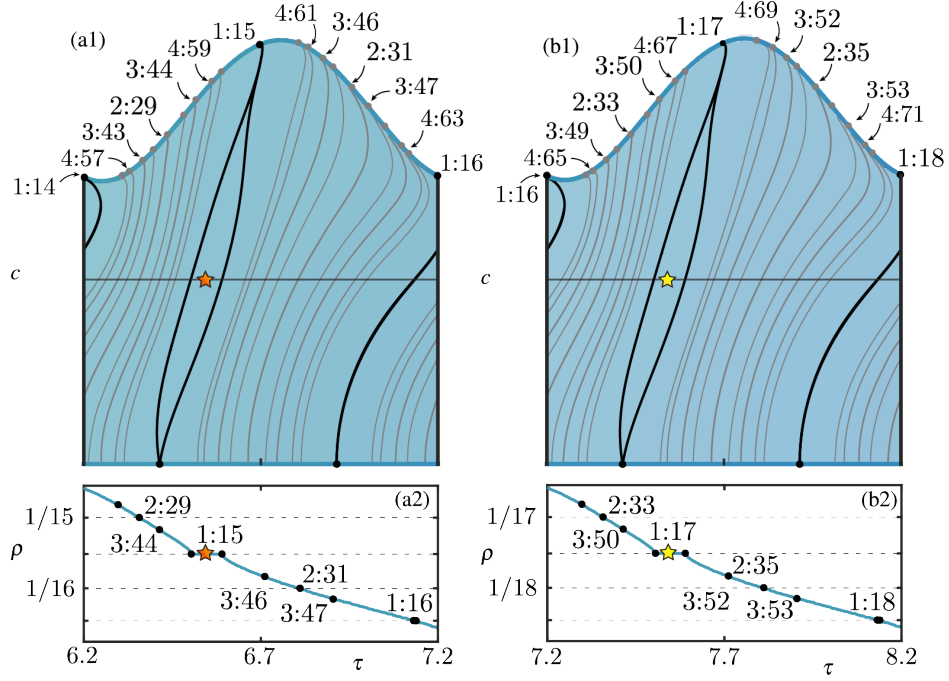


FIGURE 13. Preservation of the resonance structure under the shift $\tau \mapsto \tau + 1$, governed by the transformation Φ , illustrated for Eq. (2) with $\alpha = 1.25$. Panels (a1) and (b1) show the rotation number ρ in the (τ, c) -plane for $\tau \in [6.2, 7.2]$ and $\tau \in [7.2, 8.2]$, respectively, in the same layout as Figure 9. Panels (a2) and (b2) show slices at fixed $c = 4$, displaying the devil's staircase graph of ρ where dots indicate saddle-node bifurcations.

used steps of 0.0025 in τ for c values 0.0053 apart. The locus GT was traced by continuing a period-50 saddle locked orbit Γ_u from the zero-forcing line through the (τ, c) -plane.

6. REAPPEARANCE OF RESONANCE TONGUES FOR LARGE τ

We now discuss the periodicity observed in Figures 9 and 10 of the resonance structure with period one in τ , for sufficiently large τ . Figure 13 shows the bifurcation set and the rotation number ρ of Eq. (2) in the (τ, c) -plane with $\alpha = 1.25$ and $\omega = 2\pi$ for $\tau \in [6.2, 7.2]$ in panel (a1) and for $\tau \in [7.2, 8.2]$ in panel (b1), respectively; both are beyond τ -range in Figure 9. We overlay all $p:q$ resonance tongues of the form $1:q$ up to $5:q$, together with their roots on the torus bifurcation curves \mathbb{T} and \mathbb{T}_0 , with the rotation number ρ colored according to the colorbar provided in Figure 10. Figures 13(a2)–(b2) show associated slices at fixed $c = 4$, displaying the graph of ρ where the dots indicate the associated resonance tongues.

Comparing Figure 13(a1) and (b1), we observe a near-identical arrangement of the resonance tongues under the shift $\tau \mapsto \tau + 1$, where a $p:q$ resonance tongue appears transformed to

$$(15) \quad \Phi(p:q) = p:(q + 2p).$$

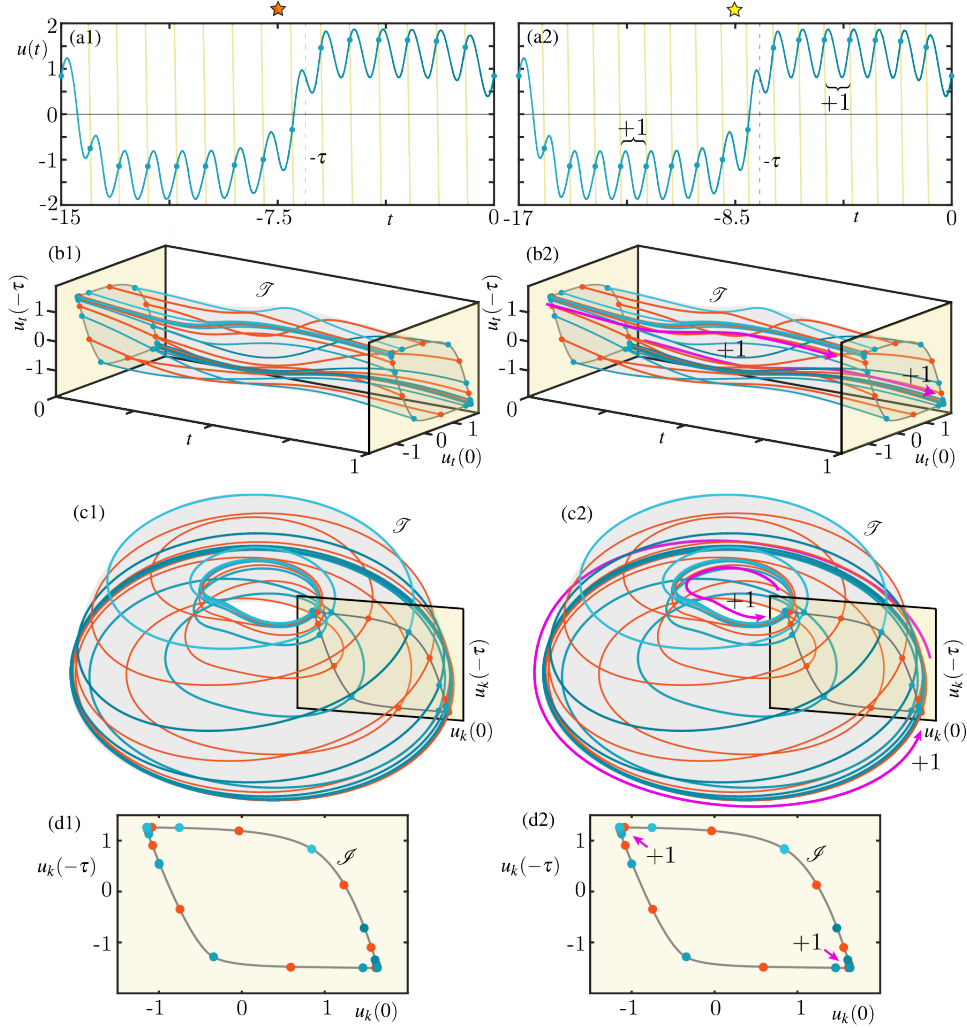


FIGURE 14. Locked orbits of Eq. (2) with $\alpha = 1.25$, $c = 4$, $\omega = 2\pi$, and delay $\tau = 6.54$ in the first column and $\tau = 7.54$ in the second column. Each row illustrates representative dynamics by showing: time series over one period (a); attracting (blue) and saddle (orange) locked orbits represented in $(t, u_t(0), u_t(-\tau))$ -space in between the planes $t = 0$ and $t = 1$ (b); a torus embedding showing these orbits, where the planes $t = 0$ and $t = 1$ are identified (c); and the headpoints of the locked orbit in the stroboscopic Poincaré section (plane at $t = 0$) in panel (d). We also show in panels (b) and (c) the unstable manifold of the saddle orbit, which forms the invariant torus \mathcal{T} (grey), and the invariant circle \mathcal{S} in panel (d).

For example, the 1:14, 2:29, and 3:44 resonance tongues are mapped to 1:16, 2:33, and 3:50, respectively. Accordingly, the graph of ρ in panel (a2) aligns with that in panel (b2), subject to (15).

To illustrate how the transformation Φ manifests at the level of individual solutions, Figure 14 compares periodic orbits of Eq. (2) for fixed $\alpha = 1.25$, $c = 4$ and $\omega = 2\pi$, for the two delays $\tau = 6.54$ and $\tau = 7.54$, shown in the left and right columns. These periodic

orbits lie within the 1:15 and $\Phi(1:15) = 1:17$ resonance tongues, respectively (indicated by the orange and yellow stars in Figure 13).

Row (a) of Figure 14 displays the time series of the attracting periodic orbit over one period, with vertical lines marking each forcing period. Rows (b)–(d) follow the same format as Figure 6: row (b) shows the attracting and saddle locked orbits together with the invariant torus \mathcal{T} in the $(t, u_t(0), u_t(-\tau))$ -space, with the planes $t = 0$ and $t = 1$; row (c) shows the torus embedded into \mathbb{R}^3 by (10); and row (d) the associated headpoints in the $(u_t(0), u_t(-\tau))$ -plane with the invariant circle \mathcal{S} .

The time series in Figure 14(a2) differs from that in panel (a1) by two additional oscillations within the period. Accordingly, there are two additional segments between the planes at $t = 0$ and $t = 1$ in panel (b2) compared to (b1). The locked periodic orbit in panel (c2) winds two additional times around the longitude direction of \mathcal{T} compared to the one in panel (c1), corresponding to two additional headpoints in panel (d2) compared to (d1).

The key observation is that Φ admits a natural algebraic interpretation via the identification of the reduced fraction $p:q$ with the integer vector $(p, q) \in \mathbb{Z} \times \mathbb{Z}$, giving the lift

$$\tilde{\Phi} \begin{pmatrix} p \\ q \end{pmatrix} = M \begin{pmatrix} p \\ q \end{pmatrix}, \text{ with } M = \begin{pmatrix} 1 & 0 \\ 2 & 1 \end{pmatrix},$$

which recovers the map (15) through $(p, q) \mapsto p:q$. Importantly, $\tilde{\Phi}$ is a linear map with $M \in \text{SL}(2, \mathbb{Z})$, the group of 2×2 integer matrices with determinant one, and this means that Φ preserves Farey addition

$$\frac{p}{q} \oplus \frac{\ell}{m} = \frac{p+\ell}{q+m},$$

since it is vector addition for $\tilde{\Phi}$. Note that since $M \in \text{SL}(2, \mathbb{Z})$, primitive integer vectors are mapped to primitive integer vectors, so reduced fractions are mapped to reduced fractions.

The matrix M has a topological interpretation: $M = L^2$, where

$$L = \begin{pmatrix} 1 & 0 \\ 1 & 1 \end{pmatrix} \in \text{SL}(2, \mathbb{Z})$$

is the standard generator of a *Dehn twist* about one of the fundamental cycles of the torus, acting as $(p, q) \mapsto (p, q + p)$; see, e.g., Chapter 3 of [20]. Hence, $M = L^2$ corresponds to two successive Dehn twists along the same cycle, and the passage $\tau \mapsto \tau + 1$ can be interpreted algebraically as a *double Dehn twist* on the torus. To visualize this, imagine slicing the torus along a longitude — much like cutting a bagel — twisting one side twice along the cut before reattaching it; see Figure 14(c).

The map Φ admits a natural extension from rational rotation numbers to all of $[0, 1]$. Indeed, the rational map (15) is given by the Möbius transformation

$$(16) \quad \Phi(\rho) = \frac{\rho}{1+2\rho},$$

which is continuous and strictly increasing on $[0, 1]$. Since the rational numbers are dense in $[0, 1]$, this uniquely determines the action of Φ on irrational rotation numbers as the continuous extension of the rational case. Note that, because $0 < \Phi(\rho) < \rho$ for all $\rho \in (0, 1]$, the rotation number ρ decreases as τ increases, in the sense that the associated resonances occur at smaller rotation numbers, which we can clearly observe in Figures 9 and 10.

We can formulate our observations as follows.

Proposition 2. *[Repeating locked and quasiperiodic orbits] Consider the pfS&S model (2) with $\omega = 2\pi$. Assume that, along the zero-forcing line $c = 0$, the model has for sufficiently large τ a normally hyperbolic attracting periodic orbit $\Gamma_s(\tau)$ whose period satisfies*

$$(17) \quad T(\tau) = 2\tau + C(\alpha) + \mathcal{O}(1/\tau), \quad \text{as } \tau \rightarrow +\infty,$$

where $C(\alpha)$ depends on α . Let

$$\rho(\tau) := \frac{1}{T(\tau)}.$$

Then, under the shift $\tau \mapsto \tau + 1$,

$$(18) \quad \rho(\tau + 1) = \Phi(\rho(\tau)) + \mathcal{O}(\rho(\tau)^3),$$

where Φ is given by (16). Consequently, the map Φ , obtained from the zero-forcing asymptotics, organizes to leading order the reappearance of locking and quasiperiodic dynamics for small periodic forcing $c > 0$.

The proof of Proposition 2 is found in Appendix B.

The appearance of the double Dehn twist follows directly from the asymptotic scaling $T(\tau) \sim 2\tau$ in Proposition 2, where the coefficient 2 reflects the symmetric periodic orbit's asymptotic square-wave structure, which traverses two slow phases per cycle. We remark that numerical evidence for the GZT model suggests an effective scaling with $n = 4$, instead yielding a quadruple Dehn twist. More generally, if the intrinsic period satisfies an asymptotic relation of the form $T(\tau) \sim n\tau$, then the corresponding transformation of rotation numbers would formally be

$$\rho \mapsto \frac{\rho}{1 + n\rho}.$$

Its restriction to rational rotation numbers lifted to $\mathbb{Z} \times \mathbb{Z}$ is given by $(p, q) \mapsto L^n(p, q)$, corresponding to n Dehn twists. We expect and conjecture that the resonance structure of any periodically forced DDE repeats for sufficiently large τ , where the corresponding matrix in $\text{SL}(2, \mathbb{Z})$ is a power of L .

Note that the reappearance phenomenon described in Proposition 2 is fundamentally different from the well-known reappearance mechanism in DDEs [61, 22]. In that setting, if a periodic orbit with period T exists at $\tau = \tau_0$, then an exact T -periodic orbit also exists near $\tau = \tau_0 + T$, often with different stability.

7. DISCUSSION AND OUTLOOK

We carried out a comprehensive bifurcation analysis of the pfS&S model (2) with a focus on its resonance structure. We began by analyzing the autonomous S&S model (1), providing a complete description of its equilibria and their stability via a linear stability analysis. With `DDE-BifTool`, we found and continued bifurcations that linear stability analysis cannot capture to complete the global bifurcation scenario. In this way, we established that, for sufficiently large delays, the sole attracting invariant structures are periodic orbits.

To assess the effect of seasonal locking, we introduced periodic forcing with angular frequency $\omega = 2\pi$ (corresponding to annual forcing, for time in years), leading to the pfS&S DDE model (2). In such a periodically forced system, the intrinsic oscillations resulting from the delayed feedback interact with the external forcing, giving rise to attracting invariant tori and resonance phenomena. We extended to the periodically forced DDE setting a method originally developed for periodically forced planar ODEs [4, 5] to compute the rotation number ρ for an attracting invariant torus. A key part of this extension involves

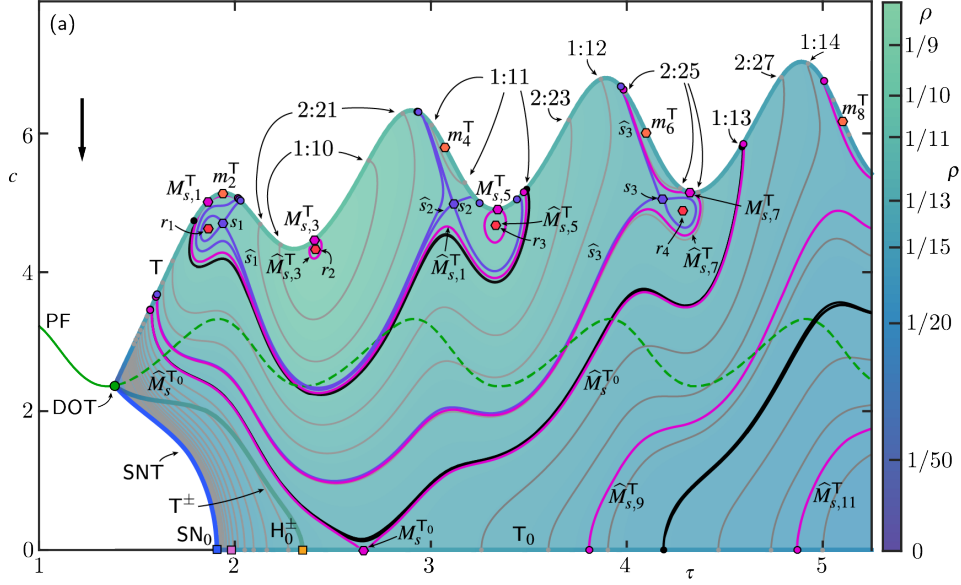


FIGURE 15. Bifurcation set and rotation number ρ of the pfVoC model in the (τ, c) -plane for $\alpha = 0.75$, $\omega = 2\pi$, and $\gamma = 0.49$. The figure follows the same format as Figure 10. Along the torus bifurcation curve T , boundary saddles $M_{s,2k-1}^T$ (pink) and boundary minima m_{2k}^T (orange) are marked, with the associated separatrices $\widehat{M}_{s,k}^T$ shown in pink. In the interior of the torus dynamics region, interior maxima r_k (red) and interior saddles s_k (purple) are marked, with associated separatrices \widehat{s}_k shown in purple.

carefully handling projection issues specific to the infinite-dimensional phase space of a DDE.

We analyzed the bifurcation diagram and resonance structure of the pfS&S model in the (τ, c) -plane for representative values of the feedback strength: the mathematically convenient case $\alpha = 1.25$ and the physically more relevant case $\alpha = 0.75$. For both, resonance tongues organize around critical points of the rotation number ρ — both along the torus bifurcation curves and in the interior of the region with an invariant torus; this is consistent with recent observations [4, 5]. We found that the resonance structure repeats for large delays as described by the rational map Φ . At the level of individual locked orbits this map Φ encodes additional winding along the longitudinal direction of the invariant torus; mathematically, it is a map on rational rotation numbers that respects the Farey tree. For $\alpha = 1.25$, there is always a unique global attractor. However, for $\alpha = 0.75$, we additionally found bistability between period-one orbits and invariant tori. The associated hysteresis scenario involves complex bifurcation sequences, including ‘saddle-node’ and ‘gluing’ bifurcations of tori. Importantly, neither regime exhibits resonance overlap and, consequently, no chaotic dynamic is observed.

As we mentioned in the introduction, Suarez and Schopf [52] derived their S&S model in an ad hoc way, but recently Falkena *et al.* [19] derived two S&S-type models from a spatially extended ENSO model more formally. The Mori–Zwanzig model lacks stable periodic orbits for most physically realistic parameter values and is therefore unsuitable for

modeling ENSO variability; we focus instead on the variation-of-constants (VoC) model:

$$(19) \quad u'(t) = u(t) - u^3(t) - \alpha u(t - \tau)(1 - \gamma u^2(t)),$$

which reduces to the classical S&S model (1) when $\gamma = 0$. For $\gamma = 0.49$, the autonomous VoC model has the same qualitative dynamical landscape as the S&S model, with bifurcation curves shifted towards larger τ ; see [19].

A natural question is how far the findings for the pfS&S model carry over to a more physically grounded model. To address this, we briefly examine the periodically forced VoC (pfVoC) model, obtained by adding the forcing term $c \cos(2\pi t)$ to (19). Figure 15 shows the bifurcation diagram of the pfVoC model in the (τ, c) -plane for $\gamma = 0.49$, $\alpha = 0.75$, and $\omega = 2\pi$, in the format of Figure 10. The pfVoC model shares the same global bifurcation structure as the pfS&S model with $\alpha = 0.75$: the region of attracting tori is bounded by the curve of torus bifurcations \mathbb{T} , \mathbb{T}_0 , and the saddle-node of tori SNT ; resonance tongues do not overlap so that ρ is continuous throughout; and the reappearance mechanism governed by (16) persists for large τ , though it is less apparent in Figure 15. This supports the conjecture that the repeating resonance structure for large τ is a typical phenomenon of periodically forced DDEs.

Despite this structural similarity, the resonance organization of the pfVoC model is considerably richer: the graph of $\rho = \rho(\tau, c)$ contains more critical points, with an alternating sequence of maxima and minima of ρ along the torus bifurcation curve \mathbb{T} , and numerous interior maxima and interior saddles in the region of attracting tori, producing a more intricate arrangement of resonance tongues and separatrices; see Figure 15 and its caption for details.

A further point of discussion concerns the role of the forcing timescale on the dynamics of the pfS&S model. As noted in the introduction, the timescale of the model is not fixed a priori and depends on many climatological parameters. On the other hand, varying ω while keeping the period in physical years fixed rescales the delay, the feedback strength, the forcing amplitude, and, more consequentially, the strength of the nonlinearities, which can promote resonance tongues overlap and lead to chaotic dynamics [11]. This is consistent with existing results: Anikushin and Romanov [3] reported positive Lyapunov exponents for trajectories at $\omega = 1$, and Oishi and Sekine [40] proved the existence of large overlapping resonance tongues for broad ranges of ω . Understanding how resonance tongues grow, interact, and overlap as ω decreases, and how the graph of ρ evolves in this process, appears to be essential for determining whether periodically forced delay models can reproduce realistic ENSO variability. In this respect, the GZT model offers a useful comparison: its timescale is fixed by construction, but it contains an explicit parameter controlling the strength of the nonlinearity, which allows one to tune the degree of resonance overlap directly. The pfS&S model lacks such a parameter, and the role of ω as a proxy for nonlinearity strength is a modeling subtlety that deserves further investigation.

Other promising extensions of the model include breaking the \mathbb{Z}_2 -symmetry of the S&S framework to capture the observed asymmetry between El Niño and La Niña events [1, 35], incorporating state-dependent delays following the approach of Keane *et al.* [28], and including stochastic forcing, which has been shown to enhance irregular variability in periodically forced delay models [63].

ACKNOWLEDGMENTS

We thank Stefan Ruschel, Courtney Quinn and Henk A. Dijkstra for their advice and insightful discussions. This research was supported by Royal Society Te Apārangi Marsden Fund grant #19-UOA-223.

DATA AVAILABILITY STATEMENT

All data are available within the article or supplemental information.

APPENDIX A. PROOF OF PROPOSITION 1

The equilibria of (1) satisfy

$$p - p^3 + \alpha p = 0,$$

so the trivial equilibrium $p_0 = 0$ exists for all (α, τ) , while

$$p^\pm = \pm\sqrt{1 - \alpha}$$

exist only when $\alpha < 1$.

For $\alpha = 1$, the equilibria p^\pm collide with p_0 . Because the system possesses a \mathbb{Z}_2 -symmetry, this is a pitchfork bifurcation $P(\tau, \alpha)$ along the line given by $\alpha = 1$, which shows (ii). The genericity conditions (involving higher-order terms) are standard and generically satisfied; see Kuznetsov [34].

Linearising (1) about an equilibrium p gives

$$y'(t) = (1 - 3p^2)y(t) - \alpha y(t - \tau).$$

At the trivial equilibrium p_0 this yields

$$(20) \quad y'(t) = y(t) - \alpha y(t - \tau),$$

with characteristic equation

$$(21) \quad \lambda = 1 - \alpha e^{-\lambda\tau}.$$

At the equilibria p^\pm we obtain

$$y'(t) = (3\alpha - 2)y(t) - \alpha y(t - \tau),$$

with characteristic equation

$$(22) \quad \lambda = 3\alpha - 2 - \alpha e^{-\lambda\tau}.$$

For $0 < \alpha < 1$, the characteristic equation (21) has one real positive root $\lambda_1 > 0$ and one real negative root $\lambda_2 < 0$, with all remaining roots having real part less than λ_2 , as shown in [3]. Hence p_0 is a saddle with a one-dimensional unstable manifold $W^u(p_0)$.

For $\alpha > 1$, we seek purely imaginary roots $\lambda = iv$ of (21). Substituting $\lambda = iv$ gives

$$\cos(v\tau) = \frac{1}{\alpha}, \quad \sin(v\tau) = \frac{v}{\alpha}.$$

Using the Pythagorean trigonometric identity yields $v^2 = \alpha^2 - 1$ which is positive for $\alpha > 1$. Writing

$$v_0 = \sqrt{\alpha^2 - 1},$$

we obtain the Hopf curves $H_k(\tau_k, \alpha)$ where

$$(23) \quad \tau_k = \frac{\arccos(1/\alpha) + 2\pi k}{v_0}, \quad k \in \mathbb{N}_0.$$

Each τ_k corresponds to a pair of eigenvalues $\pm i\nu_0$ crossing the imaginary axis. The principal branch τ_0 marks the first loss of stability of p_0 . Because p_0 is invariant under the \mathbb{Z}_2 -involution, the emanating periodic orbits satisfy (8).

For $k \geq 1$, as $\alpha \rightarrow 1^+$, the numerator of (23) converges to $2\pi k$, whereas $\nu_0 \rightarrow 0^+$, so $\tau_k \rightarrow +\infty$. Alternatively, as $\alpha \rightarrow +\infty$, the numerator converges to $\pi/2 + 2\pi k$ and $\nu_0 \rightarrow +\infty$, so $\tau_k \rightarrow 0$. This proves (i) and (iv).

For $\alpha < 1$ we analyse the characteristic equation (22). Substituting $\lambda = i\nu$ and separating real and imaginary parts gives

$$(24) \quad \cos(\nu\tau) = \frac{3\alpha - 2}{\alpha},$$

$$(25) \quad \sin(\nu\tau) = \frac{\nu}{\alpha},$$

which yields

$$\nu^2 = \alpha^2 - (3\alpha - 2)^2 = 4(1 - 2\alpha)(\alpha - 1).$$

This quantity is positive only for $\frac{1}{2} < \alpha < 1$. Writing

$$\nu_0 = 2\sqrt{(1 - 2\alpha)(\alpha - 1)},$$

we obtain

$$(26) \quad \tau_k^\pm = \frac{\arccos\left(\frac{3\alpha - 2}{\alpha}\right) + 2\pi k}{\nu_0}, \quad k \in \mathbb{N}_0.$$

Each such value corresponds to a pair of purely imaginary eigenvalues $\pm i\nu_0$. The principal branch τ_0^\pm marks the first loss of stability of p^\pm as τ increases. The emanating periodic orbits appear in symmetric pairs related by (8), corresponding to the two equilibria p^\pm .

For $k \geq 1$, as $\alpha \rightarrow 1^-$, the numerator of (26) converges to $2\pi k$, whereas $\nu_0 \rightarrow 0^+$, so $\tau_k^\pm \rightarrow +\infty$. As $\alpha \rightarrow \frac{1}{2}^+$, the numerator tends to $\pi(2k + 1)$, whereas $\nu_0 \rightarrow 0^+$, so $\tau_k^\pm \rightarrow +\infty$. This proves (iii) and (v).

Finally, rewriting (21) as

$$f(\lambda; \alpha, \tau) = 1 - \alpha e^{-\tau\lambda} - \lambda,$$

one checks that at $(\alpha, \tau) = (1, 1)$ the root $\lambda = 0$ has multiplicity two. Indeed,

$$\lim_{\lambda \rightarrow 0} \frac{f(\lambda; 1, 1)}{\lambda} = 0, \quad \lim_{\lambda \rightarrow 0} \frac{f(\lambda; 1, 1)}{\lambda^2} = -\frac{1}{2},$$

so the algebraic multiplicity is exactly two, and this establishes (vi).

We do not verify the Hopf and pitchfork nondegeneracy conditions analytically; these have been confirmed numerically in later sections using `DDE-BifTool`.

APPENDIX B. PROOF OF PROPOSITION 2

The period law (17) is motivated by a large-delay square-wave analysis of Chow–Mallet-Paret type: after rescaling time by $s = t/\tau$, the zero-forcing equation becomes a singularly perturbed delay equation whose outer solutions lie near the plateaus $\pm\sqrt{1 + \alpha}$, with rapid transitions between them. This formal picture suggests a period $T(\tau)$ of the form $2\tau + C(\alpha)$ plus some small corrections, where the constant $C(\alpha)$ is determined by an associated heteroclinic matching problem. In our computations, solving the equation with `dde23` for $\tau \in [50, 500]$ and fitting the measured periods to $T(\tau) = a_1\tau + a_2 + a_3/\tau$

consistently gives $a_1 \approx 2$, with a_2 depending on α and with only small $1/\tau$ corrections. This supports the asymptotic form (17) which gives

$$T(\tau + 1) = 2(\tau + 1) + C(\alpha) + \mathcal{O}(1/\tau) = T(\tau) + 2 + \mathcal{O}(1/\tau),$$

because both remainders at τ and $\tau + 1$ are of order $\mathcal{O}(1/\tau)$. Hence,

$$\rho(\tau + 1) = \frac{1}{T(\tau) + 2 + \mathcal{O}(1/\tau)}.$$

Since $T(\tau) = \mathcal{O}(\tau)$ and $\rho(\tau) = 1/T(\tau)$, this becomes

$$\rho(\tau + 1) = \frac{\rho(\tau)}{1 + 2\rho(\tau) + \mathcal{O}(\rho(\tau)^2)}.$$

Expanding the denominator gives

$$\rho(\tau + 1) = \frac{\rho(\tau)}{1 + 2\rho(\tau)} + \mathcal{O}(\rho(\tau)^3).$$

Thus, to leading order,

$$\rho(\tau + 1) = \Phi(\rho(\tau)), \quad \text{with } \Phi(\rho) = \frac{\rho}{1 + 2\rho}.$$

Assuming that the periodic orbit Γ_s is normally hyperbolic, it persists under sufficiently small forcing $c > 0$. Resonance tongues are then expected to emanate from rational values $\rho = p/q$ along the $c = 0$ line, corresponding to $p : q$ phase locking. Between these, one expects quasiperiodic dynamics with irrational rotation number. Hence, the map Φ , although derived from the zero-forcing asymptotics, gives the leading-order organization of the nearby forced dynamics.

REFERENCES

- [1] Soon-Il An and Fei-Fei Jin. Nonlinearity and asymmetry of ENSO. *Journal of Climate*, 17(12):2399–2412, 2004.
- [2] Mikhail Anikushin. Nonlinear semigroups for delay equations in hilbert spaces, inertial manifolds and dimension estimates. *Differential Equations and Control Processes*, 12 2022.
- [3] Mikhail Anikushin and Andrey Romanov. Hidden and unstable periodic orbits as a result of homoclinic bifurcations in the Suarez–Schopf delayed oscillator and the irregularity of ENSO. *Physica D: Nonlinear Phenomena*, 445:133653, 2023.
- [4] John Bailie and Bernd Krauskopf. Bifurcations of resonance tongues in a periodically forced model for vertical mixing in the North Atlantic Ocean. In *Proceedings of the European Nonlinear Dynamics Conference (ENOC 2024)*, Delft, The Netherlands, July 2024.
- [5] John Bailie, Priya Subramanian, and Bernd Krauskopf. Devil’s terraces: determining the organization of resonance tongues in a periodically forced dynamical system, 2026.
- [6] David S Battisti and Anthony C Hirst. Interannual variability in a tropical atmosphere–ocean model: Influence of the basic state, ocean geometry and nonlinearity. *Journal of Atmospheric Sciences*, 46(12):1687–1712, 1989.
- [7] Jeff Bezanson, Alan Edelman, Stefan Karpinski, and Viral B Shah. Julia: A fresh approach to numerical computing. *SIAM Review*, 59(1):65–98, 2017.
- [8] Jacob Bjerknes. A possible response of the atmospheric hadley circulation to equatorial anomalies of ocean temperature. *Tellus*, 18(4):820–829, 1966.
- [9] Jakob Bjerknes. Atmospheric teleconnections from the equatorial pacific. *Monthly weather review*, 97(3):163–172, 1969.
- [10] S. Bolduc-St-Aubin and Antony R. Humphries. Seasonal forcing dominated dynamics of a piecewise smooth Ghil-Zaliapin-Thompson ENSO model. *Journal of Computational Dynamics*, 15(1):113–162, 2026.
- [11] Samuel Bolduc-St-Aubin and Bernd Krauskopf. From resonance to chaos in a dde climate model. In *Proceedings of the 23rd IFAC World Congress*, Busan, Republic of Korea, August 2026. Accepted, to appear.
- [12] Ian Boutle, Richard HS Taylor, and Rudolf A Römer. El Niño and the delayed action oscillator. *American Journal of Physics*, 75(1):15–24, 2007.

- [13] Renato C. Calleja, Antony R. Humphries, and Bernd Krauskopf. Resonance phenomena in a scalar delay differential equation with two state-dependent delays. *SIAM Journal on Applied Dynamical Systems*, 16:1474–1513, 2017.
- [14] NOAA Climate Prediction Center. Weekly sst anomalies in the equatorial pacific (Niño regions). <https://www.cpc.ncep.noaa.gov/data/indices/wksst9120.for>. Accessed: 2025-05-31.
- [15] Odo Diekmann, Stephan A Van Gils, Sjoerd MV Lunel, and Hans-Otto Walther. *Delay equations: functional-, complex-, and nonlinear analysis*, volume 110. Springer Science & Business Media, 2012.
- [16] Henk A. Dijkstra. The role of conceptual models in climate research. *Physica D: Nonlinear Phenomena*, 457:133984, 2024.
- [17] Dale R Durran. The third-order adams-bashforth method: An attractive alternative to leapfrog time differencing. *Monthly weather review*, 119(3):702–720, 1991.
- [18] Valentin Duruisseau and Antony R. Humphries. Bistability, bifurcations and chaos in the Mackey-Glass equation. *Journal of Computational Dynamics*, 9(3):421, 2022.
- [19] Swinda KJ Falkena, Courtney Quinn, Jan Sieber, Jason Frank, and Henk A Dijkstra. Derivation of delay equation climate models using the mori-zwanzig formalism. *Proceedings of the Royal Society A*, 475(2227):20190075, 2019.
- [20] Benson Farb and Dan Margalit. *A primer on mapping class groups*, volume 49. Princeton University Press, 2011.
- [21] Michael Ghil, Ilya Zaliapin, and Skip Thompson. A delay differential model of ENSO variability: Parametric instability and the distribution of extremes. *Nonlinear Processes in Geophysics*, 15, 12 2007.
- [22] Andrus Giraldo and Stefan Ruschel. Pulse-adding of temporal dissipative solitons: resonant homoclinic points and the orbit flip of case B with delay. *Nonlinearity*, 36(12):7105, nov 2023.
- [23] Jack K Hale and Sjoerd M Verduyn Lunel. *Introduction to functional differential equations*, volume 99. Springer Science & Business Media, 2013.
- [24] Fei-Fei Jin. An Equatorial Ocean Recharge Paradigm for ENSO Part II: A Stripped-Down Coupled Model. *Journal of the Atmospheric Sciences.*, 54:830–847, 1997.
- [25] Fei-Fei Jin. An equatorial ocean recharge paradigm for ENSO. Part I: Conceptual model. *Journal of the Atmospheric Sciences.*, 54:811–829, 1997.
- [26] Fei-Fei Jin, J.David Neelin, and Michael Ghil. El Niño/Southern Oscillation and the annual cycle: subharmonic frequency-locking and aperiodicity. *Physica D: Nonlinear Phenomena*, 98(2):442–465, 1996. Nonlinear Phenomena in Ocean Dynamics.
- [27] Andrew Keane and Bernd Krauskopf. Chenciner bubbles and torus break-up in a periodically forced delay differential equation model. *Nonlinearity.*, 31:R165, 2018.
- [28] Andrew Keane, Bernd Krauskopf, and Henk A. Dijkstra. The effect of state dependence in a delay differential equation model for the El Niño Southern Oscillation. *Philosophical Transactions: Mathematical, Physical and Engineering Sciences.*, 377, 2019.
- [29] Andrew Keane, Bernd Krauskopf, and Claire Postlethwaite. Delayed feedback versus seasonal forcing: Resonance phenomena in an El Niño Southern Oscillation model. *SIAM Journal on Applied Dynamical Systems.*, 14:1229–1257, 2015.
- [30] Andrew Keane, Bernd Krauskopf, and Claire M. Postlethwaite. Investigating irregular behavior in a model for the El-Niño Southern Oscillation with positive and negative delayed feedback. *SIAM Journal on Applied Dynamical Systems.*, 15:1656–1689, 2016.
- [31] Andrew Keane, Bernd Krauskopf, and Claire M. Postlethwaite. Climate models with delay differential equations. *Chaos.*, 27:114309, 2017.
- [32] Bernd Krauskopf and Kirk Green. Computing unstable manifolds of periodic orbits in delay differential equations. *Journal of Computational Physics*, 186(1):230–249, 2003.
- [33] Bernd Krauskopf and Jan Sieber. Bifurcation analysis of delay-induced resonances of the El-Niño Southern Oscillation. *The Royal Society.*, 470:20140348, 2014.
- [34] Yuri A. Kuznetsov. *Elements of applied bifurcation theory*. Springer-Verlag., 2004.
- [35] Narasimhan K Larkin and DE Harrison. ENSO warm (El Niño) and cold (La Niña) event life cycles: Ocean surface anomaly patterns, their symmetries, asymmetries, and implications. *Journal of climate*, 15(10):1118–1140, 2002.
- [36] Michael J McPhaden, Stephen E Zebiak, and Michael H Glantz. ENSO as an integrating concept in earth science. *science*, 314(5806):1740–1745, 2006.
- [37] Hazime Mori. Transport, collective motion, and brownian motion. *Progress of theoretical physics*, 33(3):423–455, 1965.
- [38] M Munnich, Mark A Cane, and Stephen E Zebiak. A study of self-excited oscillations of the tropical ocean-atmosphere system. *J. Atmos. Sci.*, 48:1238–1248, 1991.

- [39] Mir Muhammad Nizamani, Alice C. Hughes, Yichao Wang, Hai-Li Zhang, and Zhongping Lai. Climate extremes and socioeconomic impact of El Niño and La Niña events. *Environmental Development*, 56:101276, 2025.
- [40] Shin'ichi Oishi and Kouta Sekine. Inclusion of periodic solutions for forced delay differential equation modeling El Niño. *Nonlinear Theory and Its Applications, IEICE*, 12:575–610, 01 2021.
- [41] John E. Oliver. *Walker Circulation*, pages 797–798. Springer Netherlands, Dordrecht, 2005.
- [42] Joël Picaut, François Masia, and Yves du Penhoat. An advective-reflective conceptual model for the oscillatory nature of the ENSO. *Science*, 277(5326):663–666, 1997.
- [43] Stefan Ruschel, Sylvain Barbay, Neil GR Broderick, and Bernd Krauskopf. Strongly resonant polarization dynamics of pulse trains in a spin-flip model for an excitable microlaser with delayed self-feedback. *The European Physical Journal Special Topics*, pages 1–13, 2025.
- [44] Pierce Ryan, Andrew Keane, and Andreas Amann. Border-collision bifurcations in a driven time-delay system. *Chaos.*, 30:1229–1257, 2020.
- [45] Tim Sauer, James A Yorke, and Martin Casdagli. Embedology. *Journal of statistical Physics*, 65(3):579–616, 1991.
- [46] L.F Shampine and S. Thompson. Solving DDEs in MATLAB. *Applied Numerical Mathematics.*, 37:441–458, 2001.
- [47] Jan Sieber, Koen Engelborghs, Tatyana Luzyanina, Giovanni Samaey, and Dirk Roose. DDE-BIFTOOL manual - bifurcation analysis of delay differential equations. <http://arxiv.org/abs/1406.7144>, 07 2014.
- [48] Jan Sieber and Bernd Krauskopf. Bifurcation analysis of an inverted pendulum with delayed feedback control near a triple-zero eigenvalue singularity. *Nonlinearity*, 17(1):85–103, 2004.
- [49] Hal Smith. *An Introduction to Delay Differential Equations with Sciences Applications to the Life*. Springer-Verlag, 2011.
- [50] Hilary Spencer. Role of the atmosphere in seasonal phase locking of El Niño. *Geophysical research letters*, 31(24), 2004.
- [51] Karl Stein, Axel Timmermann, Niklas Schneider, Fei-Fei Jin, and Malte F Stuecker. ENSO seasonal synchronization theory. *Journal of Climate*, 27(14):5285–5310, 2014.
- [52] Max J. Suarez and Paul S. Schopf. A delayed action oscillator for ENSO. *Journal of the Atmospheric Sciences.*, 45:3283–3287, 1988.
- [53] Floris Takens. Detecting strange attractors in turbulence. In *Dynamical Systems and Turbulence, Warwick 1980: proceedings of a symposium held at the University of Warwick 1979/80*, pages 366–381. Springer, 2006.
- [54] Soizic Terrien, Bernd Krauskopf, Neil GR Broderick, Venkata A Pammi, Rémy Braive, Isabelle Sagnes, Grégoire Beaudoin, Konstantinos Pantzas, and Sylvain Barbay. Merging and disconnecting resonance tongues in a pulsing excitable microlaser with delayed optical feedback. *Chaos: An Interdisciplinary Journal of Nonlinear Science*, 33(2), 2023.
- [55] The MathWorks, Inc. *MATLAB version R2024b*. The MathWorks, Inc., Natick, Massachusetts, 2024. Available at <https://www.mathworks.com/products/matlab.html>.
- [56] Kevin E Trenberth. The definition of El Niño. *Bulletin of the American Meteorological Society*, 78(12):2771–2778, 1997.
- [57] Eli Tziperman, Lewi Stone, Mark A. Cane, and Hans Jarosh. El Niño chaos: Overlapping of resonances between the seasonal cycle and the pacific ocean-atmosphere oscillator. *Science-AAAS Weekly Paper Edition-including Guide to Scientific Information*, 214:72–74, 1994.
- [58] Chunzai Wang and Joël Picaut. Understanding ENSO physics—a review. *Earth's Climate: The Ocean–Atmosphere Interaction, Geophys. Monogr.*, 147:21–48, 2004.
- [59] Chunzai Wang, Robert H Weisberg, and Jyotika I Virmani. Western pacific interannual variability associated with the El Niño–Southern Oscillation. *Journal of Geophysical Research: Oceans*, 104(C3):5131–5149, 1999.
- [60] Robert H Weisberg and Chunzai Wang. A western Pacific oscillator paradigm for the El Niño–Southern Oscillation. *Geophysical research letters*, 24(7):779–782, 1997.
- [61] S. Yanchuk and P. Perlikowski. Delay and periodicity. *Phys. Rev. E*, 79:046221, Apr 2009.
- [62] Ilya Zaliapin and Michael Ghil. A delay differential model of ENSO variability—Part 2: Phase locking, multiple solutions and dynamics of extrema. *Nonlinear Processes in Geophysics*, 17(2):123–135, 2010.
- [63] T Živković and Kristoffer Rypdal. ENSO dynamics: Low-dimensional-chaotic or stochastic? *Journal of Geophysical Research: Atmospheres*, 118(5):2161–2168, 2013.
- [64] Robert Zwanzig. Nonlinear generalized Langevin equations. *Journal of Statistical Physics*, 9(3):215–220, 1973.

DEPARTMENT OF MATHEMATICS, UNIVERSITY OF AUCKLAND, PRIVATE BAG 92019, AUCKLAND
1142, NEW ZEALAND

Email address: `sbo1082@aucklanduni.ac.nz`

DEPARTMENT OF MATHEMATICS, UNIVERSITY OF AUCKLAND, PRIVATE BAG 92019, AUCKLAND
1142, NEW ZEALAND

DEPARTMENT OF MATHEMATICS, UNIVERSITY OF AUCKLAND, PRIVATE BAG 92019, AUCKLAND
1142, NEW ZEALAND